nature methods

Article

https://doi.org/10.1038/s41592-025-02929-3

SmartEM: machine learning-guided electron microscopy

Received: 15 May 2024

Accepted: 23 October 2025

Yaron Meirovitch [1,2,10] ✉, **Ishaan Singh Chandok** [1,3,10], **Core Francisco Park** [1,3,10], **Pavel Potocek** [4,5,10], **Lu Mi** [6,7], **Shashata Sawmya** [6], **Yicong Li** [8], **Thomas L. Athey** [6], **Vladislav Susoy** [1,2], **Neha Karlupia** [1,2], **Yuelong Wu** [1,2], **Daniel R. Berger** [1,2], **Richard Schalek** [1,2], **Caitlyn A. Bishop** [9], **Daniel Xenes** [9], **Hannah Martinez** [9], **Jordan Matelsky** [9], **Brock A. Wester** [9], **Hanspeter Pfister** [1,8], **Remco Schoenmakers** [4], **Maurice Peemen** [4], **Jeff W. Lichtman** [1,2] ✉, **Aravinthan D. T. Samuel** [1,3] ✉ & **Nir Shavit** [6] ✉

Connectomics provides nanometer-resolution, synapse-level maps of neural circuits to understand brain activity and behavior. However, few researchers have access to the high-throughput electron microscopes necessary to generate enough data for whole-brain or even whole-circuit reconstruction. To date, machine learning methods have been used after the collection of images by electron microscopy (EM) to accelerate and improve neuronal segmentation, synapse reconstruction and other data analysis. With the continual computational improvements in processing EM images, acquiring EM images will become the rate-limiting step in automated connectomics. Here, in order to speed up EM imaging, we integrate machine learning into real-time image acquisition in a single-beam scanning electron microscope. This SmartEM approach allows an electron microscope to perform data-aware imaging of specimens. SmartEM saves time by allocating the proper imaging time for each region of interest—first scanning all pixels rapidly and then rescanning more slowly only the small subareas where a higher quality signal is required. We demonstrate that SmartEM achieves up to an ~7-fold acceleration of image acquisition time for connectomic samples using a commercial single-beam SEM in samples from nematodes, mice and human brain. We apply this fast imaging method to reconstruct a portion of mouse cerebral cortex with an accuracy comparable to traditional electron microscopy.

Serial-section electron microscopy is widely used to reconstruct circuit wiring diagrams in entire brains of small animals like *Caenorhabditis elegans*, *Drosophila* and zebrafish[1–5] and brain regions in mammals[6–11]. Comparing the growing numbers of connectomes of animals with different genetic backgrounds, life experiences and diseases will illuminate the anatomical nature of learning, memory and developmental plasticity, the nature of brain evolution and the kinds of anatomical abnormalities that cause neuropathology and disease[12–16].

To achieve wide-scale deployment for comparative connectomics, data acquisition and analysis pipelines need to become more widely available[17]. At present, connectome datasets are mostly acquired by the few laboratories and institutions equipped with specialized and expensive high-throughput electron microscopes such as the Transmission Electron Microscopy Camera Array 2, GridTape or the Zeiss 61- or 91-beam scanning electron microscope (SEM)[16,18,19].

Until recently, dataset acquisition had not been a limiting factor in connectomics[20]. A more substantial bottleneck had been data

A full list of affiliations appears at the end of the paper. ✉e-mail: yaron.mr@gmail.com; jeff@mcb.harvard.edu; samuel@physics.harvard.edu; shanir@csail.mit.edu

analysis: segmenting serial-section electron micrographs to reconstruct the shape and distribution of nerve fibers, identify synapses and map circuit connectivity. The most substantial bottleneck had been manual human proofreading[5]. However, recent improvements in machine learning (ML) and image analysis[21–28] have sped data analysis and reduced the need for human proofreading, creating a need for faster image acquisition. The field needs more electron microscopes to deliver datasets as fast as they can now be analyzed. One way to meet this need is to enable widely available electron microscopes, such as more affordable single-beam SEMs, to collect connectomic datasets.

On a single-beam SEM, acquisition speed is dictated by the dwell time that the electron beam spends on each pixel. For connectomics, this is typically ≳1,000 ns per pixel to ensure high-contrast tissue imaging. In comparison, the time spent moving the beam between pixels is negligible, as modern SEMs use electrostatic scan generators for rapid beam deflection[29,30]. To accelerate an SEM for connectomics, one must therefore reduce the total dwell time without losing information essential for determining the wiring diagram.

The salient measure of image accuracy for connectomics is neuronal segmentation: being able to correctly identify each neuron's border (membrane boundary and extracellular space) and correctly identify each synapse. In standard SEM, a long, uniform dwell time is used to achieve the high signal-to-noise per pixel needed for accurate segmentation. This creates a fundamental trade-off: rapid imaging can miss critical information. Although post-acquisition methods such as denoising or upsampling can improve images[31,32], they are limited by the original information content and cannot unambiguously create data that was not first acquired.

Our solution to the problem of missing information in a rapidly acquired image is to recover information during real-time microscope operation. To do this, we developed SmartEM, a pipeline that uses an efficient machine learning algorithm to identify error-prone or high-salience regions (such as synapses) from an initial, rapidly acquired image and then immediately rescans those regions at a longer dwell time. The SmartEM pipeline is effective in any context where images exhibit high spatial heterogeneity in segmentation accuracy as a function of imaging time: a fundamental characteristic of brain images where nerve fibers and synapses can vary in size and density from region to region. By creating a composite image, using longer dwell times only where needed, SmartEM achieves the accuracy of a uniform long-dwell-time acquisition with nearly the speed of a short-dwell-time scan. Our experiments yielded between ~5–7× speedup on three different connectomic datasets using two widely available SEMs, demonstrating a method to accelerate imaging not only in biology but also in material sciences and electronic circuit fabrication.

Results

Suitability of adaptive dwell times for connectomics

To establish the rationale for our connectomics pipeline by SEM—automatically applying short dwell times to most areas that are 'easy' to segment and long dwell times to fewer areas that are 'hard' to segment—we quantitatively tested how spatial heterogeneity in representative mammalian brain images affects segmentation accuracy with different dwell times. To perform these tests, we used a recent high-quality sample comprising 94 sections of mouse visual cortex[14]. We reimaged these 94 sections at 4-nm-per-pixel resolution using a Verios 5 HP SEM from Thermo Fisher Scientific at a range of fixed dwell times from 25 to 1,200 ns per pixel.

We note that when these images were originally acquired in a previous study using multibeam SEM, the dwell time was 800 ns per pixel[14]. This dwell time was determined by an expert operator and is close to the 800–1,000 ns per pixel needed for maximal segmentation accuracy for this dataset (Fig. 1a,b).

Our segmentation algorithm—mapping EM images to border predictions (EM2B) followed by a standard watershed transform—provided an objective assessment of segmentation accuracy of images collected with different dwell times. We adapted EM2B to SEM images taken with different dwell times. We automatically segmented 256 randomly selected 2,048-pixel × 1,768-pixel regions taken from the 94-section sample imaged at 14 different dwell times. Automatic segmentation with ultrafast dwell times (25 ns per pixel) produced frequent merge and split errors compared to automatic segmentation of the same regions with overly slow dwell times (1,200 ns per pixel; Fig. 1a).

To quantify segmentation accuracy, we calculated the variation of information (VI)[33] between each automatically segmented region at each shorter dwell time and the segmentation obtained at the longest dwell time (Fig. 1b). Segmentation accuracy increased with longer dwell times and saturated at 800–1,000 ns per pixel, consistent with the rule-of-thumb practice in choosing the dwell times for connectomics. At 25 ns per pixel, acquisition speed is 40× faster than at 1,000 ns per pixel, but with lower segmentation accuracy.

Brain tissue is typically heterogeneous, with some image regions easier and others harder to segment accurately (Fig. 1c,d). Thus, segmentation accuracy varied substantially from region to region. For slow dwell times (1,000 ns per pixel), segmentation accuracy was narrowly distributed around small VI, indicating fewer segmentation errors. For ultrafast dwell times (25 ns per pixel), segmentation accuracy was broadly distributed. Some regions exhibited the same low VI with both ultrafast and slow dwell times ('easy'-to-segment regions). In contrast, some regions exhibited drastically higher VI for ultrafast dwell times than slow dwell times ('hard'-to-segment regions; Fig. 1c). For each region, we determined the minimum dwell time to reach the same segmentation accuracy as that produced by the longest dwell time. We observed a broad distribution of minimum dwell times across pixel regions in this mouse cortex sample. Most 2,048-pixel × 1,768-pixel regions are accurately segmented with dwell times ≤150 ns per pixel, but some (~25%) required longer dwell times. Minimum dwell times exhibited a broad-tailed distribution from 50 to 1,200 ns per pixel (Fig. 1d).

Challenges in implementing SmartEM

We sought a SmartEM pipeline that could both identify and adapt to the spatial heterogeneity in the segmentation accuracy of brain tissue at various dwell times. Implementing such a pipeline on an SEM poses several challenges. First, the SEM needs to automatically identify regions likely to produce segmentation errors when acquired rapidly. Next, the SEM needs to slowly rescan pixel neighborhoods within and around these 'error-prone' regions to improve segmentation. Finally, the pipeline needs to accurately segment composite images built from the initial rapidly acquired images fused with rescanned error-prone regions. Below, we describe the solutions to these challenges that form our SmartEM pipeline.

To identify error-prone regions in rapidly acquired images, we developed a ML algorithm to run on the microscope's support computer. To take a particular example (Fig. 2a), a short-dwell-time scanned image produced a segmentation merge error that would have been avoided with a longer-dwell-time scan of the same tile. By use of a neural network (ERRNET; see below), it was possible to identify the error-causing location in the rapidly acquired image and specify the error-prone region to be rescanned that would remedy segmentation errors. This region includes the poorly defined cell membranes causing the merge error. ERRNET can operate in real-time within the SEM computer when equipped with a commodity GPU. This network runs faster than the short scan image acquisition (<100 ns per pixel) and can be further sped up by parallelization with multiple GPUs.

To use the prediction of error-prone regions during real-time SEM operation, we modified the scanning procedure of the microscope to rescan error-prone regions at long dwell times right after the short scan. In addition to rescanning error-prone regions, neural networks can be trained for data-aware rescan of additional regions of interest, such as

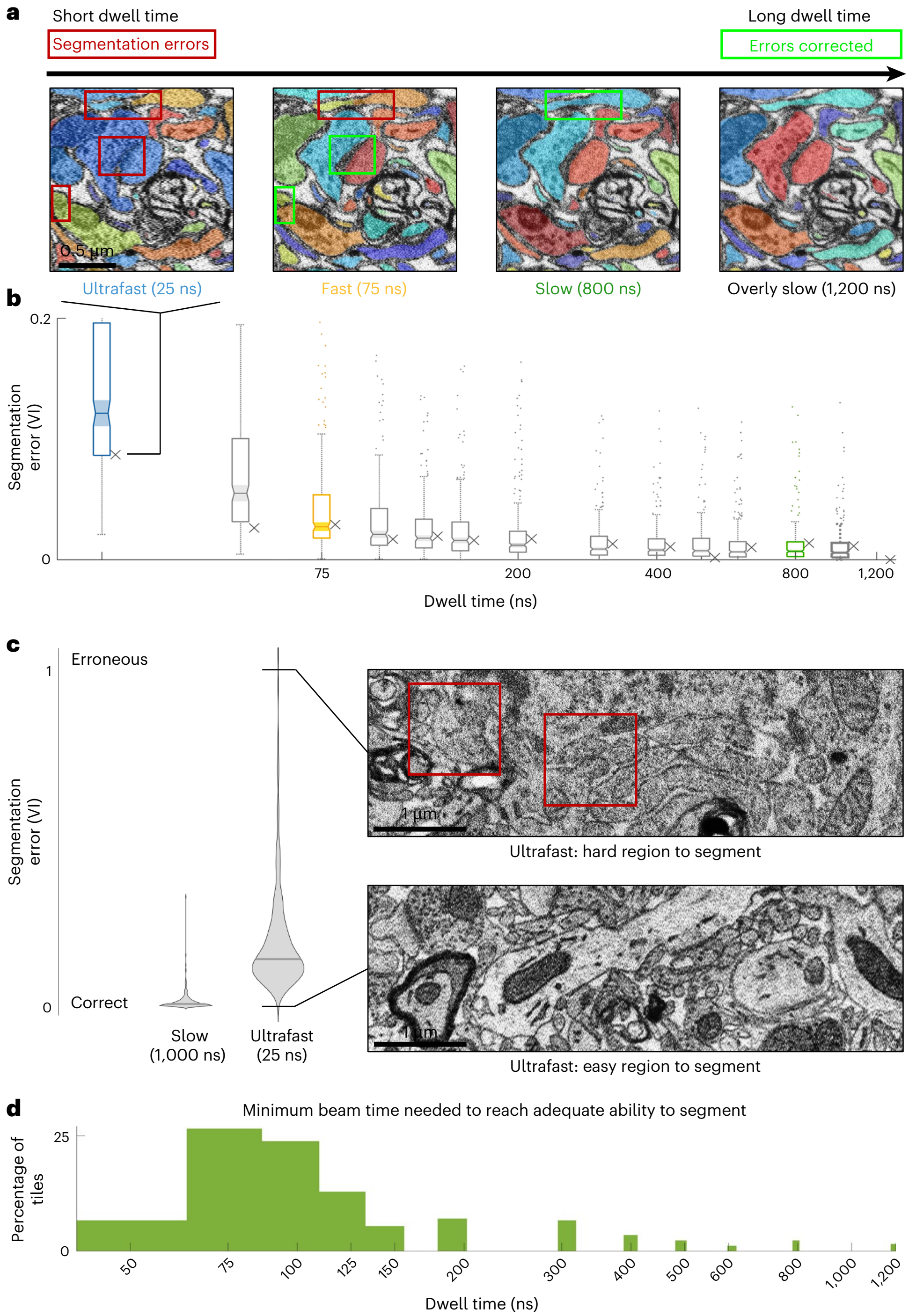

Fig. 1 | The effect of the beam's dwell time on the ability to segment the EM into neuronal elements. a, Scanning the same EM tile with different dwell times. Short-dwell-time scans result in segmentation errors (red squares) that are resolved by longer scans (green squares). **b**, The segmentation quality of the same images used in **a** are represented by × markers, alongside the distribution of segmentation qualities of 256 images (scatter and boxes) for 13 dwell times, from 25 to 1,000 ns per pixel, calculated relative to a reference image taken at 1,200 ns per pixel. Segmentation error is quantified by VI; *y* axis). Box plots show the median (center line); 25th–75th percentiles (box) and whiskers extending to the most extreme points within 1.5 × interquartile range. **c**, Comparison of segmentation error (VI) distributions for slow (1,000 ns) and ultrafast (25 ns) dwell times. Two example images, both taken at 25 ns per pixel, are shown, corresponding to a high-error case (top) and a low-error case (bottom) from the wide distribution of the ultrafast scan. **d**, Distribution of the minimum dwell time required to achieve adequate segmentation quality for 256 different image regions. The *x* axis represents the dwell time in nanoseconds per pixel, and the *y* axis represents the proportion of regions that meet the quality threshold at that specific dwell time.

synaptic clefts for applications in connectomics. We show data-aware rescans where the microscope is guided to retake regions around synaptic clefts that are predicted from an initial short scan image of a section of mammalian cortex (Fig. 2b). SEMs with electrostatic scan generators are able to conduct efficient and rapid rescans without wasted time in moving the electron beam[29,30]. When ERRNET and rescan software are seamlessly integrated within SEM computer hardware, the total time spent acquiring an image is the total number of pixels times the short initial dwell time plus the total number of rescanned pixels times their long dwell time.

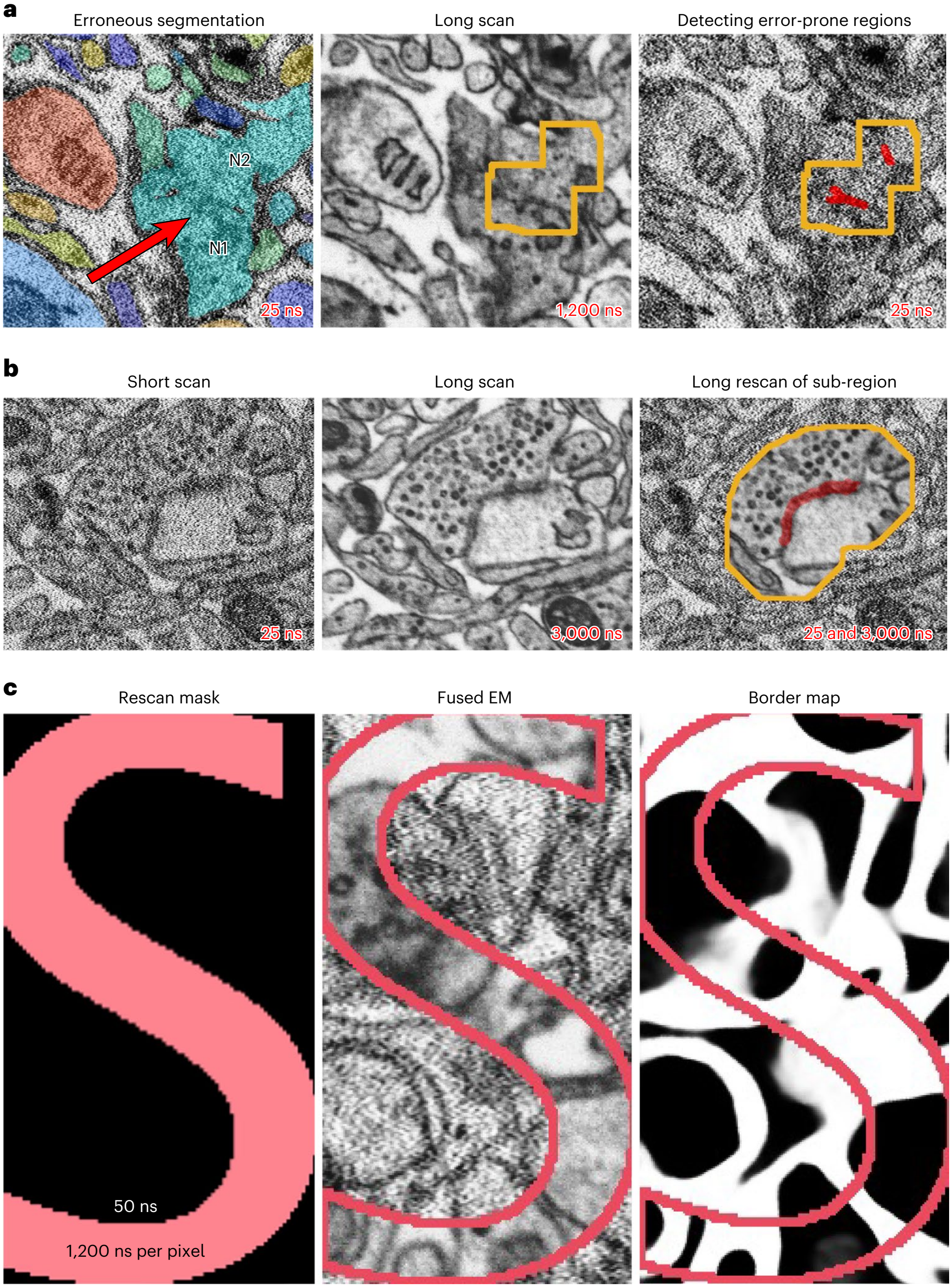

Fig. 2 | Smart microscope challenges. a, ML detecting error-prone regions. An erroneous segmentation of a rapidly acquired image (25 ns per pixel) with a red arrow indicating the location of a merge error between two neurons (N1, N2). Acquiring the same image at a long dwell time of 1,200 ns per pixel enhances the neuronal boundary (middle). The output of the ERRNET neural network that was trained to predict segmentation errors from EM is shown on the right in red (25 ns per pixel). The yellow outline is a window around the predicted error to provide further context needed for downstream correction. **b**, SEM rescanning any subregion. The SEM captures any part of an image at different dwell times, homogeneously at short dwell times (left; 25 ns per pixel), homogeneously at long dwell times (middle; 3,000 ns per pixel) or homogeneously at short dwell times with a subregion taken at long dwell times (right; 25 and 3,000 ns per pixel). Here, the yellow outline for the long-dwell-time subregion contains a synaptic cleft. **c**, ML segmenting multi-dwell-time images. Predicting neuronal borders from fused EM images using FUSEDEM2B.

After image acquisition, a smart microscopy pipeline generates a complete rapidly acquired image and set of rescanned regions of each sample acquired at longer dwell times. Composite images are produced by substituting pixels from rescanned regions into corresponding locations in the initially rapidly acquired images, resulting in images with pixels of multiple dwell times. Previous segmentation algorithms for connectomics have dealt with a single prefixed dwell time[22,24,25,34]—these algorithms generalize poorly to homogeneous images taken at different dwell times or to heterogeneous images composed of regions taken at different dwell times. The smart microscopy pipeline demands new algorithms to accurately segment composite images where different regions are obtained at different dwell times.

We developed a data-augmentation training procedure technique for a neural network with a U-Net[35–38] architecture (FUSEDEM2B) to accurately detect borders in an image with heterogeneous dwell times as well as if the image was taken with a single uniformly applied dwell time (Extended Data Fig. 1). We show an example image with multiple dwell times, where long-dwell-time scanning occurs arbitrarily within an S-shaped region surrounded by short scanning (Fig. 2c). The borders predicted by FUSEDEM2B are unperturbed when crossing between regions taken with different dwell times.

Thus, the challenges in building a smart microscopy pipeline are met by extensively using ML in both guiding image acquisition and image analysis.

The smart microscopy pipeline

We developed an integrated smart pipeline that meets the above challenges and illustrate how the pipeline operates on a small tile from the mouse cortex dataset[14] (Fig. 3). The SmartEM pipeline first establishes a target segmentation quality by determining the minimum standard dwell time required for maximal accuracy (for example, 800–1,000 ns per pixel for the mouse cortex dataset). The design and implementation of the core components of SmartEM are described below in detail.

To further reduce imaging time, we adjusted the pixel dwell time locally based on maintaining segmentation accuracy. Most image regions can be segmented with full accuracy after scanning with a short dwell time. Additional dwell time was selected only for those regions that required longer imaging to segment properly. This selection was accomplished via a neural network (ERRNET) that learned what regions required a longer dwell time after scanning whole images with a short dwell time. ERRNET learns the features of error-causing locations in raw short-dwell-time images that produce segmentation differences—erroneous merges or splits—in comparison to long-dwell-time-acquired images.

To assemble the 'ground truth' to train ERRNET, the microscope first takes a large set of images from random locations in the specimen at multiple dwell times (for example, from 25 to 1,200 ns per pixel). These images are segmented to distinctly label every contiguous neuron cross-section. Automatic labeling can be done using border probabilities, a seeding procedure and a standard region-growing algorithm such as watershed[39]. Segmented images at all dwell times are compared to reference segmented images taken with the longest dwell time (1,200 ns per pixel for the mouse cortex dataset in Fig. 1a,b, longer than needed for fully accurate segmentation with SLOWEM2B). To automatically learn segmentation discrepancies between short- and long-dwell-time images, we developed a method to produce a binary error mask that defines the morphological differences between two segmented images based on the VI clustering metric[33]. We trained ERRNET to predict error-causing regions in short-dwell-time images, as shown in Fig. 3b. We used the VI metric to detect objects that are morphologically different between segmentations of short- and long-dwell-time images and then mapped the borders that differ for these objects (Extended Data Figs. 1 and 2)[33]. We noted that all segmentation errors in short-dwell-time images can be repaired (that is, leading to segmentation identical to long-dwell-time images) by selectively replacing only regions surrounding discrepancy-causing locations in short-dwell-time images with corresponding regions taken from long-dwell-time images.

In real-time operation, the SEM must take an initial rapidly acquired image, execute ERRNET to detect error-prone locations, define a rescan mask by padding error-prone locations to capture enough context to improve segmentation accuracy and then immediately rescan all error-prone regions using longer dwell times (Fig. 3c).

Technique evaluation

We developed our SmartEM pipeline to expedite connectomics reconstruction on two widely available SEMs, the Verios 5 HP and the Magellan 400L, both from Thermo Fisher Scientific. We quantitatively estimate the practical improvement in quality and speed of this pipeline for connectomics in a variety of tissues, including reimaging a previously studied mouse cortex[14], a previously studied human temporal lobe H01 dataset[16] and a newly prepared male *C. elegans* dataset.

One premise of the smart microscopy pipeline is that automatically detecting error-prone regions and replacing them with longer-dwell-time pixels will reduce segmentation errors. To test this premise, we compared the accuracy of a segmentation pipeline trained to deal with short-dwell-time images (FASTEM2B at 100 ns per pixel) to a SmartEM pipeline trained to deal with composite images made from short and long dwell times (FUSEDEM2B at 100 ns per pixel and 2,500 ns per pixel). The performance of these networks was compared to the standard segmentation pipeline with long-dwell-time image acquisition (SLOWEM2B at 2,500 ns per pixel). For fair comparison, we used the same long dwell time for the rescanning in the SmartEM pipeline and for the uniform scan in the standard pipeline. We found that using these dwell times, SmartEM is approximately 5× faster than the standard segmentation pipeline with long-dwell-time image acquisition and approximately 2–3× more accurate (based on VI) than the standard pipeline operating quickly (100 ns per pixel) (Extended Data Fig. 3). Thus, fusing long-dwell-time pixels into a rapidly acquired image can improve segmentation accuracy.

Another premise of the SmartEM pipeline is that the additional time devoted to rescanning part of an image yields a greater improvement in segmentation accuracy than distributing the same extra time across all pixels with a uniform dwell time, as shown in Fig. 4a. To test this premise, we used a 'standard' pipeline with competitively fast settings: 400 ns per pixel for *C. elegans* and 75 ns per pixel for the mouse and human cortex datasets. We then compared these images to a SmartEM pipeline configured to match the same overall acquisition time by combining an initial short scan and a targeted longer rescan (Extended Data Fig. 4). For the three datasets, the initial SmartEM dwell time was set to 300, 50 and 50 ns per pixel, and the rescan dwell time was set to 800, 150 and 300 ns per pixel, respectively. In each case, we adaptively selected 12.5%, 16.7% and 8.33% of the most error-prone regions for rescanning to ensure that total acquisition time matched that of the standard pipeline. The procedure for selecting these SmartEM parameters for imaging is described below. We compared the VI from 123, 219 and 62 segmented image tiles of each pipeline to reference images taken at a long dwell time and found that SmartEM produced substantially fewer errors than the standard pipeline (sign tests and distributions of VI differences are in Extended Data Fig. 4).

We considered two scenarios for the large-scale collection of a connectome dataset. The first scenario involves a fixed imaging time budget to acquire a selected data volume at the selected pixel resolution. Here, the task is to intelligently allocate a fixed imaging time to optimize segmentation accuracy. The second scenario involves matching a fixed image quality to acquire a volume. Here, the task is to determine SmartEM parameters (initial dwell time, rescan dwell time and rescan rate) that maintain the quality of a given traditional dwell time while minimizing the required imaging time. Below we analyze both scenarios.

Scenario 1: Optimized accuracy with a fixed imaging time budget. In Scenario 1, we fix the total imaging time and task SmartEM with optimizing parameters (initial/rescan dwell times and rescan rate) to maximize segmentation accuracy.

We present the results of parameter optimization for different effective dwell times (smart imaging time) and across multiple datasets (Fig. 4b). This optimization links any effective dwell time (achieved by optimizing the VI for different T_{initial}, T_{rescan}) to an accuracy-equivalent standard homogeneous dwell time. For example, an effective dwell time of 150 ns per pixel in the mouse cortex dataset already attains the maximal quality using a specific set of initial, rescan dwell times and rescan rates that are determined per tile. This quality is comparable to standard homogeneous scan at 800–1,000 ns per pixel.

We show the time saved by SmartEM compared to standard microscopy (Fig. 4b). For the mouse cortex dataset, the maximal saving

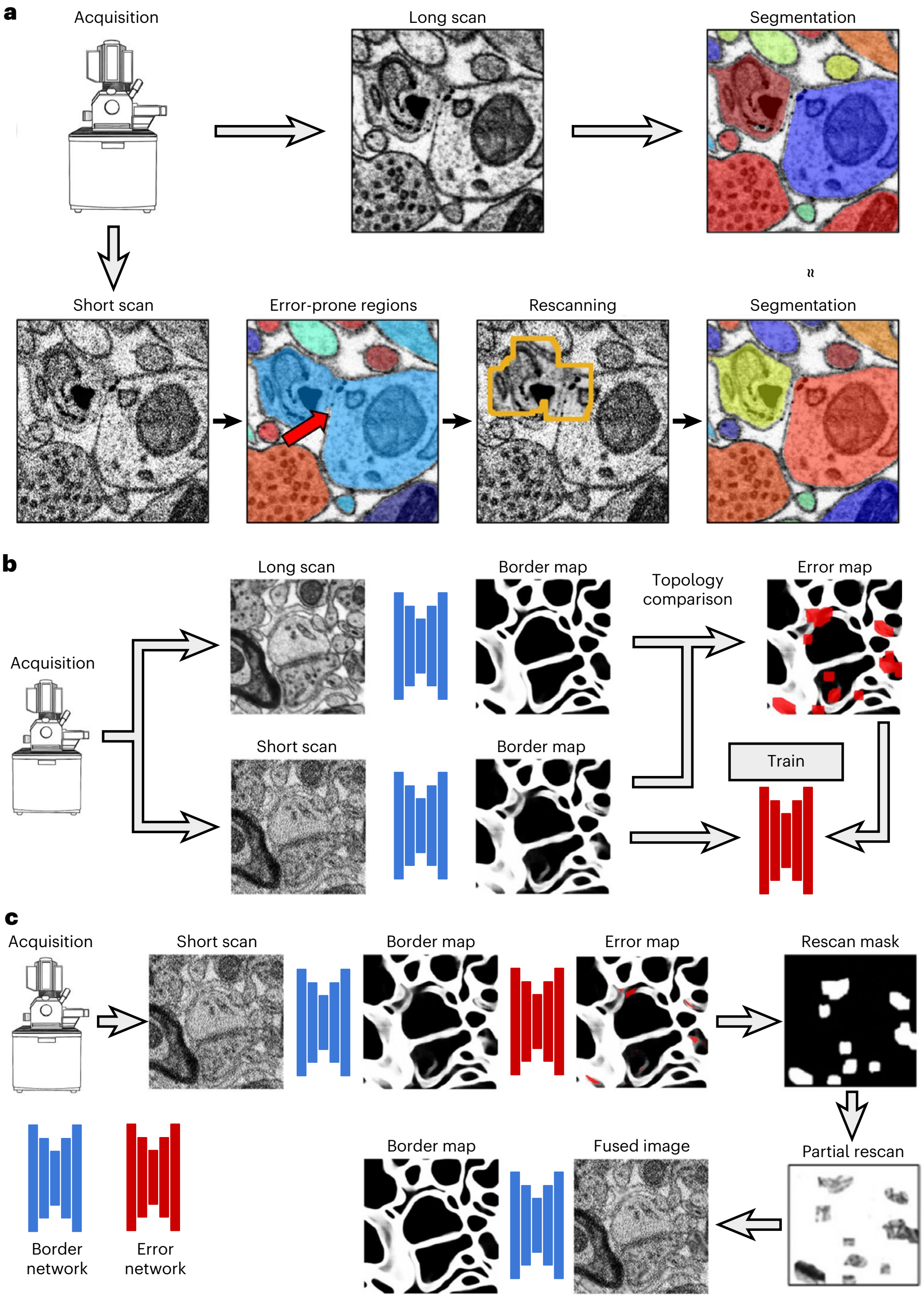

Fig. 3 | The SmartEM pipeline. **a**, Smart multistep imaging compared to standard imaging. Top: in standard EM, the sample is first scanned with a long dwell time and then segmented. Bottom: in the SmartEM pipeline, the sample is first scanned at a short dwell time, and error-prone regions are detected and rescanned and then segmented. **b**, For training, SmartEM requires aligned stacks of high-quality (long-scan) images and low-quality (short-scan) images. A border detector, FUSEDEM2B (blue), is trained on this dataset to reproduce the high-quality results of a border detector that runs only on the long-scan images. Once FUSEDEM2B is trained, the border predictions between the short and long dwell times are compared (topology comparison), and a binary error map featuring the differences between the two predictions is produced. A second network, ERRNET (red), is trained to predict this error map from the border predictions of the short-dwell-time images. **c**, For acquisition, SmartEM first performs a short scan. The trained networks FUSEDEM2B and ERRNET are used to obtain a rescan mask. This region is rescanned at a longer dwell time, resulting in a fused EM image with better segmentation quality.

compared to standard EM is achieved when SmartEM is used at an effective dwell time of ~125 ns per pixel, which corresponds to an accuracy akin to ~690 ns per pixel by the standard pipeline. This effective dwell time produces images at a speedup of ~6× with nearly maximal possible segmentation accuracy (Fig. 1). The same analysis shows that the *C. elegans* male nerve ring can be acquired at a speedup of ~5× and the human temporal lobe at a speedup of approximately ~7×.

We estimate the time to replicate the accuracy of SmartEM using standard microscopy on 1 terapixel of tissue (Fig. 4b). For the mouse cortex, the SmartEM microscope running for 42 h of continuous imaging achieves the same quality as a standard pipeline running for 212 h.

Scenario 2: Minimizing imaging time with fixed image quality. In the second scenario, a certain volume needs to be segmented while minimizing imaging cost. The total imaging time is not fixed in advance,

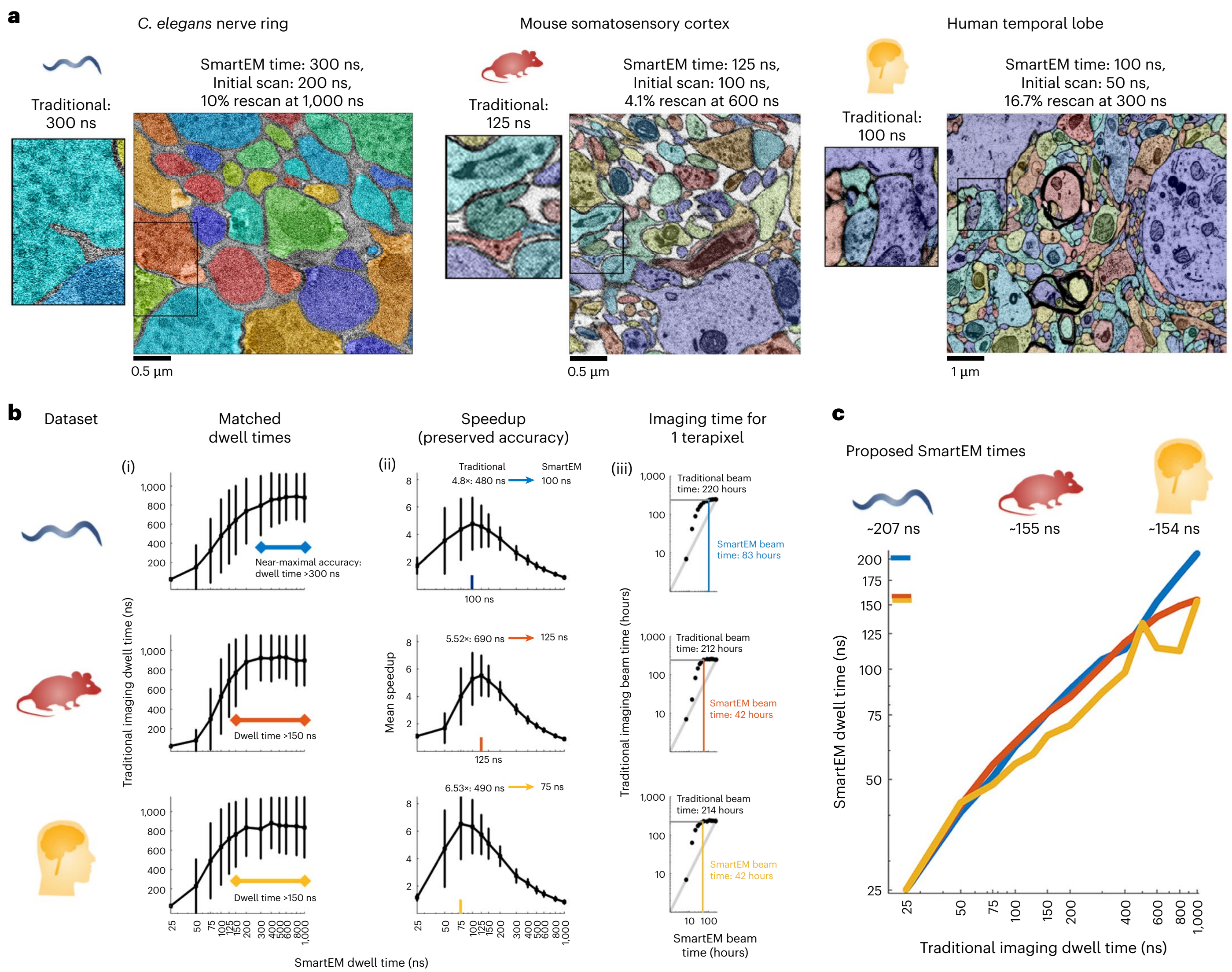

Fig. 4 | SmartEM acquisition time. a, Examples of SmartEM acquisition across three datasets: *C. elegans* nerve ring, mouse somatosensory cortex and human temporal lobe, visually compared to traditional EM imaging at the same average dwell time. **b**, Accuracy optimization for desired beam time. In the first imaging scenario, the imaging time is constrained by a fixed time budget, which, given a volume size and pixel resolution, determines the average dwell time (beam time per pixel). The task is to identify SmartEM parameters (initial dwell time, rescan dwell time and rescan rate) that optimize segmentation accuracy. (i), For each targeted effective (SmartEM) dwell time (*x* axis), we compute the optimal SmartEM parameters and determine the corresponding standard (homogeneous) dwell time (*y* axis) required to achieve the same segmentation accuracy. Error bars represent the mean ± 1 s.d. for random tiles from neuropil area (worm, $N = 123$; human, $N = 62$; mouse, $N = 219$). (ii), The resulting speedup (ratio of the homogeneous dwell time to the SmartEM dwell time) from (i). (iii), The data from (i) and (ii) illustrated for a fixed volume of 1 TB at 4 nm per pixel with a slice thickness of 30 nm. **c**, In the second imaging scenario, the desired EM quality is set by a standard pipeline's dwell time, and the goal is to identify SmartEM parameters that achieve equivalent segmentation quality in minimal imaging time. Near-maximal segmentation quality (comparable to homogeneous 1,000 ns-per-pixel scanning) is attained at roughly 207 ns per pixel (*C. elegans*, blue tick), 155 ns per pixel (mouse, red tick) and 154 ns per pixel (human, orange tick).

but the quality of the SmartEM images must still meet a standard. In practice, SmartEM acquires the volume in a way that achieves segmentation results comparable to standard EM but in substantially less time. First, the operator determines the dwell time required to achieve a specific quality under standard homogeneous scanning, which can be obtained from the SmartEM pipeline's estimate of a minimum homogeneous dwell time (Fig. 1). Once the image quality is effectively set by selecting a reference dwell time for uniform scanning, SmartEM then uses its adaptive approach to minimize the overall imaging time while maintaining comparable segmentation accuracy.

We analyzed the expected imaging time of SmartEM across the three datasets by applying the following procedure separately to each tissue. We first acquired images at multiple homogeneous dwell times ranging from 25 to 1,200 ns per pixel from the same areas. Next, we applied SmartEM, using the same error detector (ERRNET) and border prediction model (FUSEDEM2B), to produce composite dwell-time images derived from different combinations of initial dwell time, rescan dwell time and rescan rate. To match each standard homogeneous dwell time to an effective SmartEM dwell time, we identified the shortest composite dwell time that produced segmentation results statistically similar from those of the standard dwell time across tiles. We show the relationship between the targeted standard dwell time and the SmartEM dwell time with comparable accuracy (Fig. 4c).

For the mouse cortex, the highest possible quality of standard EM at 800–1,000 ns per pixel (Fig. 1) is with a smart effective dwell time of ~149–155 ns per pixel. This ~5.4–6.5× speedup from standard to SmartEM is achieved by selecting the percentage of rescanned pixels in each image tile and letting ERRNET determine rescan locations.

The *C. elegans* male nerve ring, in comparison to standard EM at 800–1,000 ns per pixel, can be acquired with a smart dwell time of ~182–207 ns per pixel (~4.4–4.8×). The human temporal lobe, compared to standard EM at 500–1,000 ns per pixel, can be acquired at a smart time of ~134–154 ns per pixel (~3.7–6.5×).

Imaging and reconstruction of mouse cortex with SmartEM

We applied SmartEM to densely reconstruct multiple portions of mouse cortex tissue. Two volumes of sizes 68 × 60 × 3 μm^3 (Fig. 5a) and 118 × 102 × 3 μm^3 (Fig. 6) and a section of size 205 × 180 μm^2 (Fig. 5b–j), were imaged at 4-nm-per-pixel resolution.

For the first volume acquisition, we used an initial dwell time of 75 ns per pixel, rescan dwell time of 800 ns per pixel and rescan rate of 10%, providing an effective dwell time of

$$T_{\mathrm{effective}} = 75 + 0.1 \times 800 = 155 \text{ ns per pixel.}$$

This average dwell time for SmartEM corresponds to a standard dwell time of ~1,000 ns per pixel for traditional microscopy (see 'Technique evaluation' section). This acquisition tested the ability to acquire, stitch and align in three-dimensional (3D) serial-section volumes.

For the second volume acquisition, we employed even more competitive SmartEM parameters with an initial dwell time of 75 ns per pixel, rescan of 800 ns per pixel and a rescan rate of 3%, providing an effective dwell time of

$$T_{\mathrm{effective}} = 75 + 0.03 \times 800 = 99 \text{ ns per pixel.}$$

For this volume, a comparison between the coregistered EM images of short dwell time and composite dwell time is available in neuroglancer[40]. This acquisition tested whether highly competitive SmartEM imaging parameters would support accurate automated neuronal reconstruction in 3D (described below).

To test the scalability of SmartEM to larger imaging grids, we acquired a section of size 205 × 180 μm^2 composed of 30 × 30 individual tiles with an initial dwell time of 75 ns per pixel, a rescan of 600 ns per pixel and a rescan rate of 10%, providing an effective dwell time of

$$T_{\mathrm{effective}} = 75 + 0.1 \times 600 = 135 \text{ ns per pixel.}$$

As mentioned above, this effective dwell time corresponds to the maximal possible speedup of SmartEM for this dataset, producing images with segmentation quality akin to standard EM at ~1,000 ns per pixel. We depict the segmentation of pipeline outputs in Fig. 5b–d (left panel in neuroglancer).

We also assessed the ability to detect synapses on short-dwell-time images (25–1,000 ns per pixel) and applied this detection to the above initial scan of 75 ns per pixel with results that are comparable to long-scan imaging, as shown in Fig. 5e,f and Extended Data Figs. 5 and 6. We show the ability of SmartEM to detect and exclude regions of no interest, where cytoplasm far from the membrane is detected from the initial scan, allowing SmartEM to force skipping of long-dwell-time scanning from these regions (Fig. 5g,h). We demonstrate the ability to translate the fused images to uniform-looking EM tiles with quality akin to long-dwell-time imaging (Fig. 5i,j and Extended Data Fig. 7; visualized in neuroglancer).

To validate SmartEM for connectomics, we tested whether the resulting image volumes support accurate 3D automated reconstruction and proofreading. We first focus our analysis to the problems of neuron reconstruction. We applied a lightweight 3D neuron segmentation algorithm to the mouse cortex volume acquired at a competitive average dwell time of 99 ns per pixel (visualized in neuroglancer). We assessed the quality of resulting SmartEM image volume with automated reconstruction of fine processes and expert manual annotation (Fig. 6b), as described below.

Connectomes can contain 'split' errors (fragmenting the volume of one cell) or 'merge' errors (joining the volume of two cells). Because a comprehensive analysis of merge errors typically requires larger reconstructed volumes to assess metrics such as error-free run-length, we qualitatively inspected and verified that none of the large segmented objects was implicated in catastrophic merge errors (Fig. 6c). Spines are the fine processes that protrude from dendrites and contain synapses. To further benchmark SmartEM performance quantitatively, we studied split errors in the 3D reconstruction of dendritic spines, a challenging feature for automated reconstruction. We randomly selected three dendrites (Fig. 6b). We counted spines that were fully automatically reconstructed without split errors and spines with split errors. Expert human annotators verified every correct reconstruction and verified that every split error was correctable with proofreading. The percentage of correct spines was approximately 58%, 53% and 75% in the three dendrites. The combined percentage of correct spines was 65%, comparable to the rate of correct spine capture in recent automated reconstruction of human cortex (67%)[16].

In addition to validating the quality of automated neuron reconstruction in the mouse cortex volume, as described above, we also trained a neural network to automatically reconstructed synapses and validated the results against expert manual annotation (Fig. 6d and neuroglancer). We measured object-wise synapse precision, recall and the $F1$-score in 3D. When evaluated on the test dataset, we obtained a precision of 93.2%, a recall of 94.1% and an $F1$-score of 93.7%, comparable to state-of-the-art performance on traditional EM volumes[41,42].

Discussion

Recent advances in ML will likely shift the bottleneck in connectomics from image analysis to data acquisition. The SmartEM approach directly addresses this challenge by integrating computational intelligence into single-beam SEMs. Implemented on commodity hardware, SmartEM transforms widely available single-beam SEMs into high-throughput platforms with minimal hardware modification. Beyond accelerating imaging acquisition, SmartEM's computational framework is adaptable to different microscopy modalities, enabling intelligent, data-aware imaging in various scientific fields (see below).

A strength of SmartEM is its flexibility. The pipeline's core components—error prediction with ERRNET, real-time targeted rescanning and segmentation of composite images with FUSEDEM2B—are modular. For instance, ERRNET can be trained using any segmentation algorithm to detect errors based on user-defined metrics, not just the VI used here. This adaptability allows laboratories to integrate their preferred analysis tools and tailor the pipeline to diverse sample preparations and scientific questions.

SmartEM can improve the efficiency and accuracy of SEM image acquisition in any context where it is beneficial to selectively adjust imaging time across different regions. Analogous to foveal vision[43], SmartEM performs a rapid, wide-field scan and then selectively rescans only the information-critical areas at higher fidelity. SEM is widely used in materials science and manufacturing, where samples often have regions varying substantially in detail and complexity. These applications, as well as others where specific structural features can be predicted but not accurately reconstructed from an initial rapid scan, are suited to SmartEM. Imaging approaches that take advantage of electron beam-sensitive materials, such as cryo-EM, could also benefit from the selective rescanning of SmartEM. Sparsely distributed structures or molecules of interest can first be rapidly identified and then selectively rescanned at longer dwell time, reducing overall beam exposure while enhancing image quality.

Although we focused on neuronal reconstruction for connectomics, SmartEM was also adapted to selectively rescan high-quality images of salient structures such as chemical synapses, providing morphological reconstructions without substantial increases in total imaging time. Likewise, SmartEM can be readily adapted for applications in cell

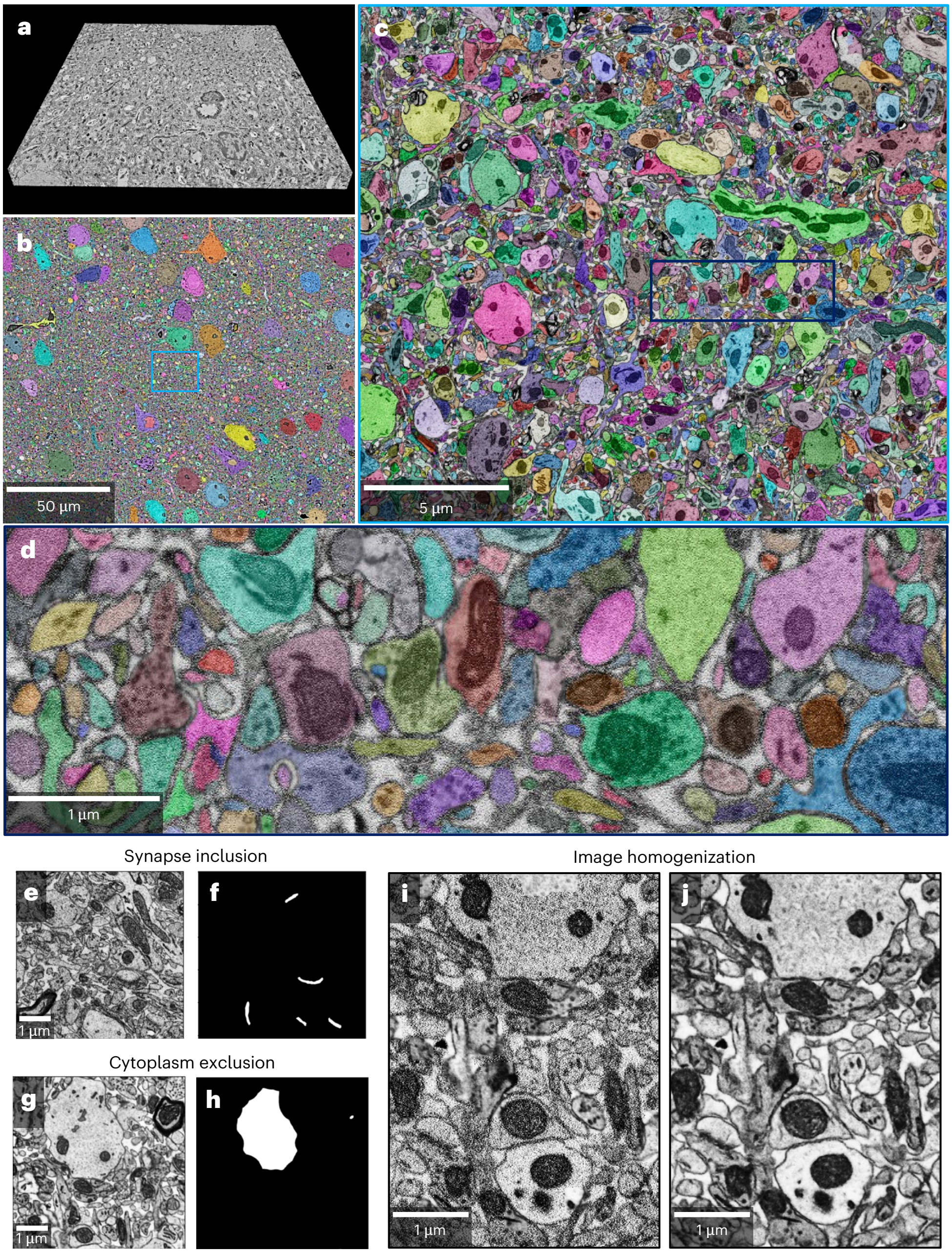

Fig. 5 | Segmentation of mouse cortex using SmartEM. a, Stitched and aligned SmartEM volume of size 68 × 60 × 3 µm^3 (94 sections) (neuroglancer). **b**, Segmentation of a single stitched SmartEM section of size 205 × 180 µm^2 using FUSEDEM2B and watershed transform (left panel in neuroglancer). **c**, Location of the highlighted region in **b** with respect to the total section. **d**, Detailed depiction of segmentation in the boxed region in **c**. **e**,**f**, Automatic detection of synapses (**f**) from a short-dwell-time image (**e**). **g**,**h**, Automatic detection of regions to be excluded (**h**) from a short-dwell-time image (**g**). **i**,**j**, An image (**i**) made of composite dwell times is stylized to appear akin to a homogeneous dwell time image (**j**). A comparison between composite dwell time and homogenized images is available in neuroglancer.

biology or pathology by selectively recognizing and rescanning other sparse but biologically important structures, such as mitochondria or other organelles.

The pipeline can also be trained to increase efficiency by excluding regions of non-interest from rescans. For example, in invertebrates like *C. elegans*, where neural tissue constitutes a small fraction of a cross-section, SmartEM can automatically focus imaging time on the nerve ring, eliminating the need for laborious manual annotation of regions of interest.

Instead of collecting serial sections on tape, one can use block-face imaging with serial tissue removal. One block-face approach, focused ion beam SEM (FIB-SEM), has distinct advantages over tape-based serial-section sample collection, including thinner tissue layers (4–8 nm) and better preservation of image alignment[44]. The primary disadvantage of FIB-SEM is its slow acquisition speed. SmartEM could mitigate this by accelerating the imaging step, enabling the collection of larger volumes in continuous runs and making block-face techniques like FIB-SEM and serial block-face SEM[45] more practical for large-scale connectomics. SmartEM is expected to provide greater speedup on block-face imaging because the imaging component is a larger part of the entire acquisition pipeline compared to serial-section SEM. Similar benefits will be obtained with other block-face imaging approaches such as serial block-face SEM where a diamond knife slices the specimen[45].

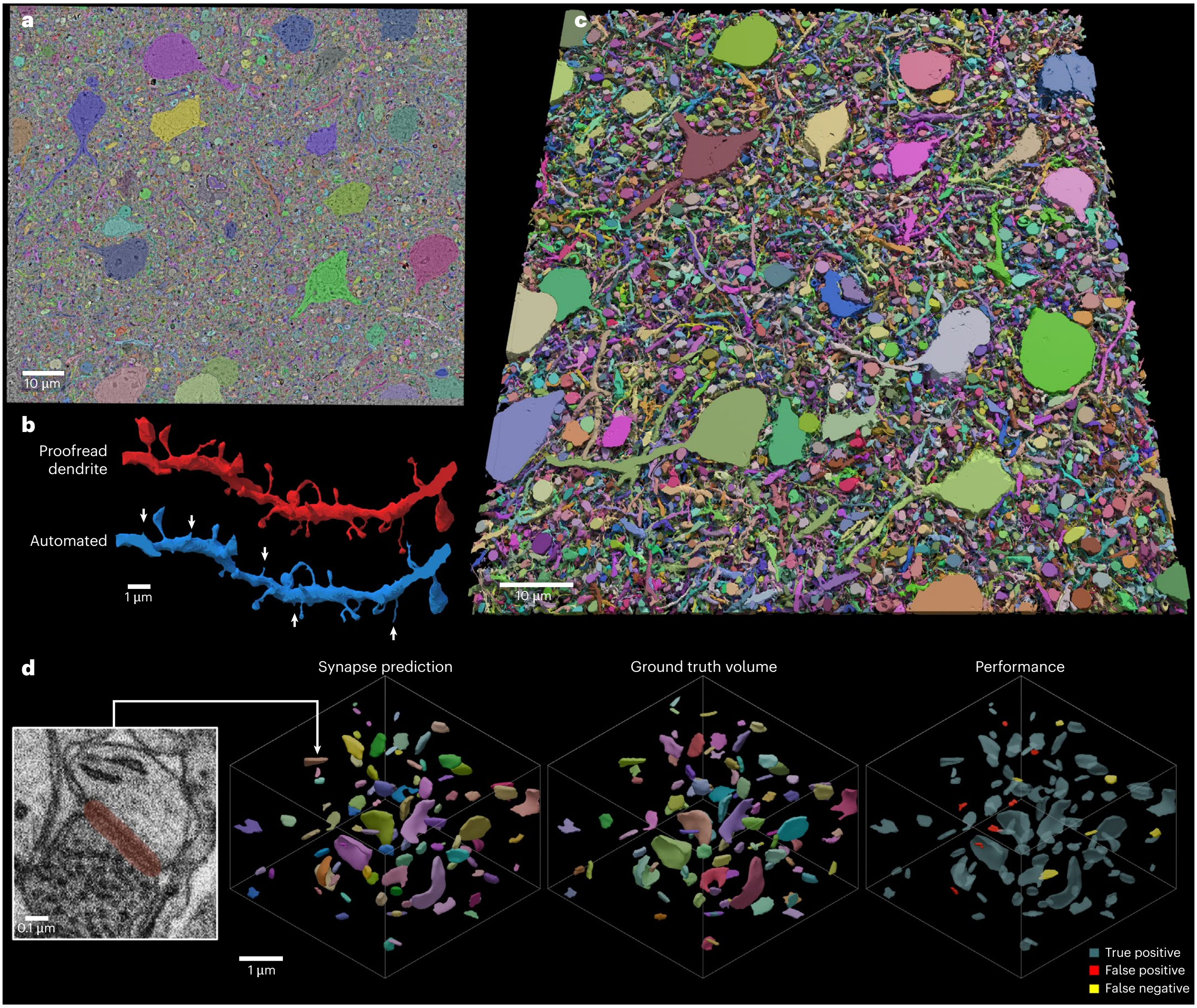

Fig. 6 | Neuronal and synapse reconstruction of a mouse cortex SmartEM volume taken at an average time of 99 ns per pixel. a, A section showing overlay of fused EM and an automated neuronal reconstruction, long- and short-dwell-time pixels at 800 ns per pixel (T_{rescan}) and 75 ns per pixel (T_{initial}), respectively, and a rescan rate of 3% (α). **b**, A dendrite reconstruction proofread by an expert (red) achieved by manually itemizing and reconstructing all dendritic spines from the fused EM image stack. An automated reconstruction (blue) achieves a high reconstruction rate of the dendritic spines. Arrowheads indicate split errors. **c**, A rendering of the automated 3D reconstruction of all sections in the dataset (94 sections). The reconstruction can be viewed in neuroglancer. **d**, Smoothed renderings of synapses showing the neural network prediction (left), expert ground truth (center) and a comparison (right). In the comparison, true positives ($N = 96$) are labeled in opaque light blue, false positives ($N = 7$) in red and false negatives ($N = 6$) in yellow. Synapse network predictions and ground truth can be visualized in neuroglancer.

Future improvements could yield even greater speedups. Leveraging 3D context from adjacent sections could reduce redundant rescans[27,46,47]. In addition, intelligently adjusting spatial resolution for different regions of tissue could further optimize beam time. These strategies can establish fast single-beam SEMs as a powerful and accessible alternative to multibeam systems for connectomics. An active area of current research is accelerating the end-to-end pipeline by parallelizing the ML with imaging and using larger fields of view[48]. We note that commercial multibeam SEMs, with their multiple beams controlled synchronously, cannot directly leverage some of these SmartEM strategies. Nonetheless, our innovations could substantially accelerate single-beam SEMs, positioning them as a viable alternative to the currently used high-throughput electron microscopes for connectomics.

Online content

Any methods, additional references, Nature Portfolio reporting summaries, source data, extended data, supplementary information, acknowledgements, peer review information; details of author contributions and competing interests; and statements of data and code availability are available at https://doi.org/10.1038/s41592-025-02929-3.

References

1. White, J. G., Southgate, E., Thomson, J. N. & Brenner, S. The structure of the nervous system of the nematode Caenorhabditis elegans. *Philos. Trans. R. Soc. Lond. B Biol. Sci.* **314**, 1–340 (1986).
2. Hildebrand, D. G. C. et al. Whole-brain serial-section electron microscopy in larval zebrafish. *Nature* **545**, 345–349 (2017).

3. Witvliet, D. et al. Connectomes across development reveal principles of brain maturation. *Nature* **596**, 257–261 (2021).
4. Winding, M. et al. The connectome of an insect brain. *Science* **379**, eadd9330 (2023).
5. Dorkenwald, S. et al. Neuronal wiring diagram of an adult brain. *Nature* **634**, 124–138 (2024).
6. Bock, D. D. et al. Network anatomy and in vivo physiology of visual cortical neurons. *Nature* **471**, 177–182 (2011).
7. Kasthuri, N. et al. Saturated reconstruction of a volume of neocortex. *Cell* **162**, 648–661 (2015).
8. Morgan, J. L., Berger, D. R., Wetzel, A. W. & Lichtman, J. W. The fuzzy logic of network connectivity in mouse visual thalamus. *Cell* **165**, 192–206 (2016).
9. Abbott, L. F. et al. The mind of a mouse. *Cell* **182**, 1372–1376 (2020).
10. Lu, X. et al. A scalable staining strategy for whole-brain connectomics. Preprint at *bioRxiv* https://doi.org/10.1101/2023.09.26.558265 (2023).
11. Song, K., Feng, Z. & Helmstaedter, M. High-contrast en bloc staining of mouse whole-brain and human brain samples for EM-based connectomics. *Nat. Methods* **20**, 836–840 (2023).
12. Rother, A., Januszewski, M., Jain, V., Fee, M. S. & Kornfeld, J. The songbird basal ganglia connectome Preprint at *bioRxiv* https://doi.org/10.1101/2025.10.25.684569 (2020).
13. Loomba, S. et al. Connectomic comparison of mouse and human cortex. *Science* **377**, eabo0924 (2022).
14. Karlupia, N. et al. Immersion fixation and staining of multicubic millimeter volumes for electron microscopy-based connectomics of human brain biopsies. *Biol. Psychiatry* **94**, 352–360 (2023).
15. Bidel, F. et al. Connectomics of the *Octopus vulgaris* vertical lobe provides insight into conserved and novel principles of a memory acquisition network. *eLife* **12**, e84257 (2023).
16. Shapson-Coe, A. et al. A petavoxel fragment of human cerebral cortex reconstructed at nanoscale resolution. *Science* **384**, eadk4858 (2024).
17. Swanson, L. W. & Lichtman, J. W. From Cajal to connectome and beyond. *Annu. Rev. Neurosci.* **39**, 197–216 (2016).
18. Zheng, Z. et al. A complete electron microscopy volume of the brain of adult drosophila melanogaster. *Cell* **174**, 730–743 (2018).
19. Phelps, J. S. et al. Reconstruction of motor control circuits in adult drosophila using automated transmission electron microscopy. *Cell* **184**, 759–774 (2021).
20. Lichtman, J. W., Pfister, H. & Shavit, N. The big data challenges of connectomics. *Nat. Neurosci.* **17**, 1448–1454 (2014).
21. Beier, T. et al. Multicut brings automated neurite segmentation closer to human performance. *Nat. Methods* **14**, 101–102 (2017).
22. Januszewski, M. et al. High-precision automated reconstruction of neurons with flood-filling networks. *Nat. Methods* **15**, 605–610 (2018).
23. Lee, K. et al. Convolutional nets for reconstructing neural circuits from brain images acquired by serial section electron microscopy. *Curr. Opin. Neurobiol.* **55**, 188–198 (2019).
24. Meirovitch, Y. et al. Cross-classification clustering: an efficient multi-object tracking technique for 3-d instance segmentation in connectomics. In *Proc. IEEE/CVF Conference on Computer Vision and Pattern Recognition* 8425–8435 (IEEE, 2019).
25. Sheridan, A. et al. Local shape descriptors for neuron segmentation. *Nat. Methods* **20**, 295–303 (2023).
26. Popovych, S. et al. Petascale pipeline for precise alignment of images from serial section electron microscopy. *Nat. Commun.* **15**, 289 (2024).
27. Celii, B. et al. Neurd offers automated proofreading and feature extraction for connectomics. *Nature* **640**, 487–496 (2025).
28. Januszewski, M., Templier, T., Hayworth, K., Peale, D. & Hess, H. Accelerating neuron reconstruction with PATHFINDER. Preprint at *bioRxiv* https://doi.org/10.1101/2025.05.16.654254 (2025).
29. Anderson, H.S., Ilic-Helms, J., Rohrer, B., Wheeler, J. & Larson, K. Sparse imaging for fast electron microscopy. In *Proc. IS&T/SPIE Electronic Imaging* (eds Bouman, C. A. et al.) 86570C-1–86570C-12 (SPIE, 2013).
30. Mohammed, A. & Abdullah, A. Scanning electron microscopy (SEM): a review. In *Proc. 2018 International Conference on Hydraulics and Pneumatics—HERVEX* (eds Matache, G. et al.) 77–85 (Hydraulics and Pneumatics Research Institute, 2018).
31. Minnen, D. et al. Denoising-based image compression for connectomics. Preprint at *bioRxiv* https://doi.org/10.1101/2021.05.29.445828 (2021).
32. Fang, L. et al. Deep learning-based point-scanning super-resolution imaging. *Nat. Methods* **18**, 406–416 (2021).
33. Meila, M. Comparing clusterings by the variation of information. In *Learning Theory and Kernel Machines, Proc. 16th Annual Conference on Computational Learning Theory and 7th Kernel Workshop, COLT/Kernel* (eds Schölkopf, B. & Warmuth, M. K.) 173–187 (Springer, 2003).
34. Lee, K., Zung, J., Li, P., Jain, V. & Seung, H.S. Superhuman accuracy on the snemi3d connectomics challenge. Preprint at https://arxiv.org/abs/1706.00120(2017).
35. Ronneberger, O., Fischer, P. & Brox, T. U-net: convolutional networks for biomedical image segmentation. In *Proc. International Conference on Medical Image Computing and Computer-Assisted Intervention* (eds Navab, N. et al.) 234–241 (Springer, 2015).
36. Ioffe, S. & Szegedy, C. Batch normalization: accelerating deep network training by reducing internal covariate shift. In *Proc. 32nd International Conference on Machine Learning* (eds Bach, F. & Blei, D.) 448–456 (PMLR, 2015); https://proceedings.mlr.press/v37/ioffe15.html
37. He, K., Zhang, X., Ren, S. & Sun, J. Deep residual learning for image recognition. In *Proc. IEEE Conference on Computer Vision and Pattern Recognition (CVPR)* 770–778 (IEEE, 2016); https://doi.org/10.1109/CVPR.2016.90
38. Kingma, D. P. & Ba, J. Adam: a method for stochastic optimization. In *Proc. International Conference on Learning Representations (ICLR)* (ICLR, 2015).
39. Vincent, L. & Soille, P. Watersheds in digital spaces: an efficient algorithm based on immersion simulations. *IEEE Trans. Pattern Anal. Mach. Intell.* **13**, 583–598 (1991).
40. Maitin-Shepard, J. et al. google/neuroglancer. *Zenodo* https://doi.org/10.5281/zenodo.5573294 (2021).
41. Turner, N. L. et al. Synaptic partner assignment using attentional voxel association networks. In *Proc. 17th IEEE International Symposium on Biomedical Imaging (ISBI)* 1–5 (IEEE, 2020); https://doi.org/10.1109/ISBI45749.2020.9098489
42. Bae, J. A. et al. Functional connectomics spanning multiple areas of mouse visual cortex. *Nature* **640**, 435–447 (2025).
43. Thorpe, S., Fize, D. & Marlot, C. Speed of processing in the human visual system. *Nature* **381**, 520–522 (1996).
44. Knott, G., Marchman, H., Wall, D. & Lich, B. Serial section scanning electron microscopy of adult brain tissue using focused ion beam milling. *J. Neurosci.* **28**, 2959–2964 (2008).
45. Denk, W. & Horstmann, H. Serial block-face scanning electron microscopy to reconstruct three-dimensional tissue nanostructure. *PLoS Biol.* **2**, e329 (2004).
46. Rolnick, D. et al. Morphological error detection in 3D segmentations. Preprint at https://arxiv.org/abs/1705.10882 (2017).
47. Zung, J., Tartavull, I., Lee, K. & Seung, H. S. An error detection and correction framework for connectomics. In *Proc. 31st Annual Conference on Neural Information Processing Systems* (eds Guyon, I. et al.) 6818–6829 (NeurIPS, 2017).
48. Athey, T. et al. Analysis of smart imaging runtime. *Appl. Microsc.* **55**, 10 (2025).

---

[1] Center for Brain Science, Harvard University, Cambridge, MA, USA. [2] Department of Molecular and Cellular Biology, Harvard University, Cambridge, MA, USA. [3] Department of Physics, Harvard University, Cambridge, MA, USA. [4] Thermo Fisher Scientific, Eindhoven, the Netherlands. [5] Saarland University, Saarbrücken, Germany. [6] Computer Science and Artificial Intelligence Laboratory, Massachusetts Institute of Technology, Cambridge, MA, USA. [7] Allen Institute for Brain Science, Seattle, WA, USA. [8] Harvard John A. Paulson School of Engineering and Applied Sciences, Harvard University, Boston, MA, USA. [9] Research and Exploratory Development Department, Johns Hopkins University Applied Physics Laboratory, Laurel, MD, USA. [10] These authors contributed equally: Yaron Meirovitch, Ishaan Singh Chandok, Core Francisco Park, Pavel Potocek. ✉e-mail: yaron.mr@gmail.com; jeff@mcb.harvard.edu; samuel@physics.harvard.edu; shanir@csail.mit.edu

Methods

Segmenting composite images

The smart microscope should be able to analyze images composed from multiple dwell times (Figs. 1c, 2b,c, 3 and 5a–d). We tested whether replacing error-prone regions in a short-dwell-time image with regions taken from long-dwell-time images improves segmentation outcomes. Extended Data Fig. 3 depicts the segmentation outcome of a short-dwell-time image taken at 100 ns per pixel segmented with a dedicated 100 ns per pixel network FASTEM2B (Extended Data Fig. 3a,e) and by FUSEDEM2B (Extended Data Fig. 3b,f). The segmentation quality of these networks are similar (top panel; VI = 0.025 and VI = 0.022). In most scenarios, the network trained to deal with fused EM (FUSEDEM2B) produces better results than networks trained to handle a fixed dwell time, even if the input into the two networks consists of a single homogeneous dwell time. Extended Data Fig. 3c,g depicts the segmentation of an image where the error-prone regions were detected by an error detector and replaced with long-dwell-time pixels (2,500 ns). The error level is typically and substantially cut by ~3–4×. The 2,500-ns-per-pixel reference image and its segmentation are shown in Extended Data Fig. 3d,h. All error estimates based on VI shown in Extended Data Fig. 3 are presented as the sum of the merge-error term and split-error term.

Imaging procedure

The SEM is automated to acquire images of individual tiles of every specimen section that are eventually stitched and aligned to form a total image volume (Fig. 3). The microscope navigates through multiple specimen sections held on tape and defines every specimen region of interest (S-ROI). Each S-ROI is captured at high spatial resolution by multi-tile acquisition. To identify the S-ROI and automate stage position and rotation control, we used SEM Navigator, a custom interface akin to earlier WaferMapper software[49]. The list of S-ROIs is exported into a text file, which is subsequently processed by the SmartEM pipeline (coded in Python/Matlab) using the Thermo Fisher Scientific Autoscript package (https://www.thermofisher.com/us/en/home/electron-microscopy/products/software-em-3d-vis/autoscript-4-software.html). The SmartEM pipeline controls the microscope and moves to S-ROI and individual tile positions, controlling the entire acquisition sequence.

For all image acquisitions, we used the Ultra High Resolution imaging mode with 4-nm-per-pixel spatial resolution and ~4-mm working distance. Image contrast was obtained using a back-scattered electron detector with 2,000-V stage bias. The initial short-dwell-time scan was obtained using the full-frame-acquisition Autoscript interface. The subsequent long-dwell-time rescan utilized the standard interface of Autoscript patterning.

To optimize image quality and tuning time for both short movements between neighboring tiles and long movements neighboring sections, we customized sequences of various autofunctions. These autofunctions included auto-contrast/brightness, auto-focus, auto-stigmation, auto-focus/stigmation and auto-lens alignment.

Because we used different interfaces for the initial short-dwell-time scan and long-dwell-time rescan, an additional alignment procedure was necessary to achieve pixel-resolution precision in the rescan. The basic system configuration for the rescan acquisition is described in ref. 50.

When the rescan long dwell time was shorter than ~500 ns per pixel, an unavoidable artifact due to limited system response of the electron deflection system occurred at the edge of rescan regions. We excised this artifact by omitting a 1-pixel boundary from every rescan region.

Segmentation quality metric

To compare the segmentation quality of different samples, we used a VI metric[33]. In principle, all comparisons that we made in this study can be accomplished with other metrics of segmentation quality as long as they can be applied to two-dimensional (2D) images. We expect the choice of segmentation metric to have little effect as long as any metric assesses topological attributes similar to VI (that is, whether objects are split or merged). Our implementation of the VI running on CPU/GPU is available at https://pypi.org/project/python-voi/.

Using VI to build ERRNET. To train the error detectors, we needed to locate the specific regions that contribute to the largest segmentation differences between image pairs, which is not provided by the VI metric. VI combines split and merge errors. The two error measures are defined by comparing the entropy of three segmented images[33], $S_1 \in L_1^N$, $S_2 \in L_2^N$ and $S_1 \times S_2 \in L_1^N \times L_2^N$, for two N-pixel labeling (instance segmentation) S_1 and S_2 that needs to be compared, where the Ls represents the sets of pixel labels. The segmented image $S_1 \times S_2$ is labeled by concatenating the labels from S_1 and S_2 for each pixel. The VI is then the sum of two error terms $\mathrm{VI}_{\mathrm{merge}}$ and $\mathrm{VI}_{\mathrm{split}}$

$$\begin{aligned}\mathrm{VI}_{\mathrm{merge}} &= H(S_1 \times S_2) - H(S_1),\\ \mathrm{VI}_{\mathrm{split}} &= H(S_1 \times S_2) - H(S_2),\\ \mathrm{VI} &= \mathrm{VI}_{\mathrm{merge}} + \mathrm{VI}_{\mathrm{split}}.\end{aligned} \tag{1}$$

Due to the additivity of the entropy measure[33], $\mathrm{VI}_{\mathrm{merge}}$ and $\mathrm{VI}_{\mathrm{split}}$ can be broken into individual constituents, representing the amount of error contributed by each individual label in each segmentation. We could thus rank objects in each segmentation according to the amount of variation they contribute to overall VI (Supplementary Fig. 1). The error contributed by the set of pixels that are both in segment $s_1 \in S_1$ and $s_2 \in S_2$ (that is, the error contributed by a segment in $S_1 \times S_2$) is

$$W(s_1 \cap s_2) - W(s_1)$$

and

$$W(s_1 \cap s_2) - W(s_2),$$

for the split and merge errors, respectively, where $W(A) = -\frac{|A|}{N} \times \log \frac{|A|}{N}$, $|A|$ is the number of pixels in A and N is the number of pixels in the image.

Once the substantially incompatible objects are detected in each segmentation, we used image processing to delineate the borders that are responsible for the topological differences between the two segmented images (Extended Data Fig. 2). We then produced binary masks from these errors and trained neural networks (ERRNET) to detect them directly from border probability maps, themselves produced by another neural network (FASTEM2B). Detecting borders allows our technique to disregard small 'cosmetic' variations between two segmentations that do not cause meaningful topological differences.

Standard dwell time for high accuracy segmentation

The goal of the SmartEM pipeline is to reach the same segmentation accuracy as a standard SEM when using a uniform long-dwell-time scanning regime, but acquiring the images in much less time. To accurately assess the improvement of SmartEM over a standard SEM imaging regime, we needed first to determine the shortest uniform dwell time that leads to accurate segmentation (for example, 800–1,000 ns per pixel in the example in Fig. 1b).

To accomplish this, we trained a neural network called SLOWEM2B to perform automatic border prediction in long-dwell-time-acquired images. We collected a diverse subset of long-dwell-time images from random locations in a specimen, typically twenty 5 × 5 μm^2 tiles, and performed manual segmentation by an expert to create training data for SLOWEM2B.

Next, we used SLOWEM2B to train a different neural network called EM2B that was capable of predicting borders with either long- or short-dwell-time images. Because the SEM allowed for reimaging the same regions at different dwell times, it was possible to guide the microscope to collect a large sample of EM images from different random locations in the specimen, using different dwell times ranging from 25 to 2,500 ns per pixel, as shown in Fig. 3. SLOWEM2B was applied to the long-dwell-time image at each location to automatically create segmentations that we could use as ‘ground truth’ to train EM2B to predict segmentations in both long- and short-dwell-time images. Both SLOWEM2B and EM2B were implemented using a U-Net architecture.

SLOWEM2B and EM2B calculated the trade-off between pixel dwell time and segmentation accuracy. EM2B was used to automatically segment all dwell-time images (for example, from 25 to 1,000 ns per pixel for the mouse cortex dataset) and compare them to a reference automatic segmentation corresponding to the longest-dwell-time image (for example, 1,200 ns per pixel image). Thus, it was possible to identify the shortest dwell time for which mean accuracy across tiles was not further improved by longer-dwell-time imaging. This minimum dwell time was defined by SmartEM as the required dwell time to achieve agreement with the longest-dwell-time segmentation.

Determination of maximal segmentation quality. We developed an unbiased estimate for the minimal dwell needed for 2D segmentation. We compared segmentations from N images for each pair of dwell times $d_1 < d_2$ and an overly slow dwell time d_{ref}. We asked whether the VI of the d_2 images was significantly smaller ($P < 0.05$; Wilcoxon signed-rank test) than d_1 images compared to d_{ref} images. When two dwell times were not sufficiently different, we called them equivalent. We defined the minimum dwell time with near-maximal segmentation ability as that dwell time beyond which VI does not improve.

Image normalization and augmentation

To train the FUSEDEM2B network, we used the CLAHE[51] normalization with clipLimit = 3 to bring all images to a common color space. We used on-the-fly rotation, flip, translation to augment the images in the training set. Although images are naturally 2,048 × 1,768, we subsampled 256 × 256 squares to train the network. To allow the network to deal with images with multiple dwell times, we randomly replaced patches at random locations with different dwell times (Extended Data Fig. 1). Specifically, each sample was generated by choosing a baseline image at a single dwell time and replacing up to 30 patches with a maximum size of 11 × 11 pixels with the corresponding pixels of an image with longer dwell time. To train ERRNET, we normalized border probabilities to [0,1] as an input to the network. We used the same procedure for on-the-fly translation and rotation but did not replace patches.

Accuracy optimization with fixed time budget

We fixed the total imaging time budget for a given specimen. From this requirement, the pixel dwell time was determined after subtracting overhead factors (such as image focusing, astigmatism correction and mechanical stage movement) from the total budget. For example, the user might need to image a given specimen—100 × 100 × 100 μm^3 tissue, cut in 30-nm-thick sections, imaged at 4-nm spatial resolution—within 5 days of continuous EM operation. These constraints determine the average dwell time per pixel:

$$\frac{(5\times 24\times 3{,}600\ \text{sec})(4^2\times 30\ \text{nm}^3)}{(100\ \mu\text{m})^3} = 207.36\ \text{ns per pixel.}$$

For a standard EM pipeline, 207.36 ns per pixel becomes the homogeneous pixel dwell time. For the SmartEM pipeline, the initial scan and rescan of all error-prone regions should sum to an average of 207.36 ns per pixel. This average dwell time, which we call effective dwell time, can be achieved with different combinations of initial dwell time, rescan dwell time and percentage of rescanned pixels:

$$T_{\text{effective}} = T_{\text{initial}} + \alpha \times T_{\text{rescan}}$$

where T represents dwell times.

For example, an effective average dwell time of 207.6 ns per pixel is achieved with an initial dwell time of $T_{\text{initial}} = 100$ ns per pixel, rescan rate of $\alpha = 5\%$ and rescan dwell time of $T_{\text{rescan}} = (207.36 - 100)/0.05 = 2{,}147.2$ ns per pixel. These parameter settings correspond to a specific segmentation accuracy (VI) relative to the reference homogeneous long-scan image. SmartEM considers a grid of parameter settings and calculates the T_{initial}, T_{rescan} and α settings that produce maximal accuracy (minimal VI) compared to the segmentation of reference tiles, while guaranteeing the effective dwell time.

Optional image homogenization

The SmartEM pipeline produces composite image with pixels acquired at different dwell times. A human observer will note contrast differences at interfaces between pixels with different dwell times. To increase human image interpretability, we built an image translator component that homogenizes SmartEM images to look like standard EM images with uniform dwell times. Extended Data Fig. 7 shows a specific example: a fused EM image that is a mosaic of subimages with different dwell times. To mitigate dwell-time contrasts and produce a visually coherent image, we applied a conditional generative adversarial network (IMAGEHOMOGENIZER, cGANs)[52]. Previous studies used deep learning to improve the quality of microscopy images[32,53–55], denoise EM images[31] and perform image reconstruction across different modalities[56]. IMAGEHOMOGENIZER contains two convolutional neural networks (CNNs): a generator and a discriminator[57]. Training data are a composite image and a uniformly long-dwell-time image, where the composite image is generated by randomly combining pixels from short-dwell-time and long-dwell-time images in different proportions (Fig. 5b–d, where the composite images consist of 75- and 600-ns-per-pixel dwell times). As shown in Supplementary Fig. 5, during the training process, the generator translates the simulated composite images to resemble long-dwell-time images, and the discriminator attempts to distinguish the translated images from real long-dwell-time images. The training process utilizes L1 loss and adversarial loss. After image homogenization by the generator, the fused EM images are more suitable for human inspection and retain the visual details of fine ultrastructure (Extended Data Fig. 7).

Synapse segmentation and neuronal reconstruction

Neuron reconstruction technique. To reconstruct neurons in 3D, we applied a lightweight segmentation method that we previously used to reconstruct neurons from the same sample imaged by a multi-beam SEM[14] and tissue prepared using a whole-mouse-brain-staining technique[10]. First, pixels straddling intracellular spaces were predicted by a CNN, based on the pretrained FUSEDEM2B network. To improve the network accuracy, we fine-tuned FUSEDEM2B using thirty-six 1,024 × 1,024 SmartEM tiles obtained from random locations in the target volume and annotated by an expert. Predictions from FUSEDEM2B were used as a starting point for the annotation process of the training set. All sections were segmented in 2D using the fine-tuned network and watersheds[58]. Second, a CNN was trained to predict from the EM the medial axis of all objects in 2D. This process required no additional human annotation. Third, 2D object segments were agglomerated across sections based on shape alignment and similarity. In addition, 2D segments were agglomerated if their medial axes were well-aligned using a fixed threshold determining large overlaps. Fourth, agglomerated objects containing a large number of adjacent 2D segments were flagged as objects with possible merge errors. This was done by building a regional adjacency graph whose nodes were 2D segments and edges represented spatial adjacency. Then these objects were reagglomerated iteratively from the original 2D object segments until the merge-error criterion was attained using an iterative clustering technique[59]. Fifth, orphans were detected and connected to other orphans or non-orphan objects based on their best estimate from the agglomeration graph: that is, connecting them to objects that did not pass the agglomeration threshold in the first iteration. The results of the reconstruction are shown in Fig. 6c.

Criterion for filtering dendritic spines. Three dendrites were randomly selected for quantitative analysis. We defined correctly segmented spines as spines whose segmentation included their synapse-containing regions. Incorrectly segmented spines were split errors that occurred before the synaptic region. To avoid confusing spines with dendritic filopodia, we excluded putative spines from analysis if no potential synapse was contained in the image volume. We observed three types of error: Type 1 errors occurred when the spine was prematurely truncated by a split error that occurred before the spine's corresponding synapse that was not due to an obvious image artifact (for example, tissue preparation, folds in the section). Type 2 errors occurred when the spine was not tracked at all due to a split error at its base on the dendrite that was not due to an obvious image artifact. Type 3 errors occurred when the spine was lost due to an obvious artifact. We observed such errors caused by local aberrations in tissue preparation in sections 56, 65, 66, 77 and 88. The distribution of incorrect spines and their corresponding error type is shown in Supplementary Table 1. To characterize only errors that might be associated with the SmartEM technique, we excluded the rate of Type 3 errors from consideration.

Synapse reconstruction technique. Synaptic active zones were manually segmented in VAST[60] and agreed upon by two expert annotators. Two ground-truth volumes, GT1 and GT2, were generated, of sizes $7 \times 3.5 \times 3\ \mu m^3$ and $4 \times 4 \times 3\ \mu m^3$, respectively. A U-Net was trained on GT1 to predict active zones from EM images via the PyTorch Connectomics library[61,62]. To avoid edge effects, the trained network was applied on a padded version of the EM from GT2. A threshold of 0.8 was applied to the outputs of this network, followed by 3D connected components with 26-connectivity using the cc3d library[63]. We removed segments that were smaller than 400 voxels. All parameters for post-processing were determined without studying the statistics of GT2; the voxel threshold was obtained by rounding down the smallest segment size in GT1. The results were finally cropped to account for the fact that the EM input was padded.

Validating synapse reconstruction. To assess synapse segmentability, we replicated CONFIRMS[64,65], a quantification tool developed for EM pipeline validation. In short, synapse segments were converted into keypoints by determining the location of their centroid and matched according to the distances between these keypoints. The matches were manually verified in neuroglancer. When the matching algorithm incorrectly assigned a synapse a certain label (for example, a synapse was assigned false positive when it was really a true positive), it was corrected by experts. We made corrections conservatively to the results of the matching algorithm. For example, if expert annotators saw a false positive but believed it to be an ambiguous synapse, it was still treated as a false positive. The precision, recall and *F*1-scores were calculated after these corrections were made.

Image stitching and alignment

The stitching and alignment of the sample volume were performed on composite dwell-time images. After applying a band-pass filter to raw images, we used conventional block-matching technique to obtain matching points between neighboring images, from which elastic transformations mapping the raw data to the aligned volume were computed by mesh relaxation. Code for stitching and alignment is available on GitHub at https://github.com/YuelongWu/feabas. We applied the same stitching and alignment transformations to the fast, composite and homogenized images to produce three sets of final volumes.

Sample preparation

Three samples were used in our experiments. These were (1) a previously studied mouse cortex[14], (2) a previously studied human temporal lobe[16]) and (3) a high-pressure-frozen male *C. elegans*. The preparation of the male *C. elegans* is described as follows. Several *C. elegans* males were transferred from a mixed-culture plate (N2 wildtype strain) to a separate plate seeded with *E. coli* OP50, where they were kept for 16 h before high-pressure freezing. L4 larvae were selected, and they all became adults by the time of high-pressure freezing. For high-pressure freezing, we used gold-coated copper carriers (16770152 and 16770153, Leica), which were soaked in a 2% lecithin in chloroform solution and allowed to dry to render their surface non-stick[66]. Live *C. elegans* males were transferred from the culture plate to the carrier together with a small amount of *E. coli* substrate. The samples were then frozen using a high-pressure freezer (EM ICE, Leica). This was followed by freeze-substitution, which was carried out in a programmable unit (EM AFS2, Leica) using a solution of 1% ddH2O, 1% OsO4 and 1% glutaraldehyde in acetone at −90 °C for 48 h, after which the temperature was increased by 5 C° per hour until it reached 20 °C (ref. 67). The sample pellets were then washed with acetone (three times) and infiltrated with 50% Epon in acetone for 1 h, 75% Epon in acetone overnight and 100% Epon for 1 h (the last step was repeated twice) and finally cured at 60 °C. The samples were imaged with microCT to check for major cracks. Thirty-five-nm sections were cut and collected on kapton tape using a Leica EM UC6 ultramicrotome and ATUM section collecting device[7,68]. The tape with the sections was mounted on silicon wafers, and the sections were then post-stained with uranyl acetate and lead citrate as described in ref. 68. The samples were kept under vacuum for at least 24 h before imaging to minimize any beam-related damage due to residual water.

Statistics and reproducibility

All statistical tests were done using the Wilcoxon signed-rank test for paired samples. The test was used to assess the cases where two dwell times produce similar segmentation quality by comparing the VI of individual samples to a single reference taken at a longer dwell time.

Reporting summary

Further information on research design is available in the Nature Portfolio Reporting Summary linked to this article.

Data availability

All SmartEM datasets and ML models are publicly available via a BossDB Project Page (The Brain Observatory Storage Service and Database) at https://bossdb.org/project/meirovitch2025 (ref. 69).

Code availability

All code necessary to implement SmartEM has been made available via GitHub at https://github.com/cfpark00/SmartEM under an MIT License.

References

49. Hayworth, K. J. et al. Imaging atum ultrathin section libraries with wafermapper: a multi-scale approach to EM reconstruction of neural circuits. *Front. Neural Circuits* **8**, 68 (2014).
50. Potocek, P. Adaptive specimen image acquisition using an artificial neural network. US patent 10,928,335 (2021).
51. Pizer, S. M., Johnston, R. E., Ericksen, J. P., Yankaskas, B. C. & Muller, K. E. Contrast-limited adaptive histogram equalization: speed and effectiveness. In *Proc. 1st Conference on Visualization in Biomedical Computing* (eds Höhne, K. H. & Pizer, S. M.) 337–345 (IEEE, 1990).
52. Mirza, M. & Osindero, S. Conditional generative adversarial nets. Preprint at https://arxiv.org/abs/1411.1784 (2014).

53. Wang, H. et al. Deep learning enables cross-modality super-resolution in fluorescence microscopy. *Nat. Methods* **16**, 103–110 (2019).
54. Weigert, M. et al. Content-aware image restoration: pushing the limits of fluorescence microscopy. *Nat. Methods* **15**, 1090–1097 (2018).
55. Mi, L. et al. Learning guided electron microscopy with active acquisition. In *Proc. Medical Image Computing and Computer Assisted Intervention* (eds Martel, A. L. et al.) 77–87 (Springer, 2020).
56. Li, Y. et al. X-ray2em: uncertainty-aware cross-modality image reconstruction from X-ray to electron microscopy in connectomics. In *Proc. 20th IEEE International Symposium on Biomedical Imaging (ISBI)* 1–5 (IEEE, 2023); https://doi.org/10.1109/ISBI53787.2023.10230759 (2023).
57. Isola, P., Zhu, J. Y., Zhou, T. & Efros, A. A. Image-to-image translation with conditional adversarial networks. In *Proc. IEEE Conference on Computer Vision and Pattern Recognition (CVPR)* 5967–5976 (IEEE, 2017).
58. Pavarino, E. C. et al. mEMbrain: an interactive deep learning MATLAB tool for connectomic segmentation on commodity desktops. *Front. Neural Circuits* **17**, 952921 (2023).
59. Bailoni, A. et al. Gasp, a generalized framework for agglomerative clustering of signed graphs and its application to instance segmentation. In *Proc. IEEE/CVF Conference on Computer Vision and Pattern Recognition* 11645–11655 (IEEE, 2022).
60. Berger, D. R., Seung, H. S. & Lichtman, J. W. Vast (volume annotation and segmentation tool): efficient manual and semi-automatic labeling of large 3D image stacks. *Front. Neural Circuits* **12**, 88 (2018).
61. Lin, Z., Wei, D., Lichtman, J. & Pfister, H. Pytorch connectomics: a scalable and flexible segmentation framework for EM connectomics. Preprint at https://arxiv.org/abs/2112.05754 (2021).
62. Paszke, A. et al. PyTorch: an imperative style, high-performance deep learning library. In *Proc. Neural Information Processing Systems (NeurIPS)* 8024–8035 (Curran Associates, Inc., 2019).
63. Silversmith, W. cc3d: connected components on multilabel 3D & 2D images. *Zenodo* https://doi.org/10.5281/zenodo.5719536 (2021).
64. Bishop, C. et al. CONFIRMS: a toolkit for scalable, black box connectome assessment and investigation. In *Proc. 43rd Annual International Conference of the IEEE Engineering in Medicine & Biology Society (EMBC)* 2444–2450 (IEEE, 2021); https://doi.org/10.1109/EMBC46164.2021.9630109
65. Xenes, D. et al. Neuvue: a framework and workflows for high-throughput electron microscopy connectomics proofreading. Preprint at *bioRxiv* https://doi.org/10.1101/2022.07.18.500521 (2022).
66. Mulcahy, B. et al. A pipeline for volume electron microscopy of the Caenorhabditis elegans nervous system. *Front. Neural Circuits* **12**, 94 (2018).
67. Weir, K., Dupre, C., van Giesen, L., Lee, A. S.-Y. & Bellono, N. W. A molecular filter for the cnidarian stinging response. *eLife* **9**, e57578 (2020).
68. Baena, V., Schalek, R. L., Lichtman, J. W. & Terasaki, M. in *Three-Dimensional Electron Microscopy*, vol. 152 of *Methods in Cell Biology* (eds Müller-Reichert, T. & Pigino, G.) Ch. 3 (Academic, 2019).
69. Hider, R. et al. The brain observatory storage service and database (bossdb): a cloud-native approach for petascale neuroscience discovery. *Front. Neuroinform.* **16**, 828787 (2022).

Acknowledgements

Research reported in this paper was supported by the NIH BRAIN Initiative under grant no. U01NS132158 (awarded to A.D.T.S., J.W.L., N.S., H.P. and B.A.W.) and by NIH grant nos. 5U24NS109102 (awarded to J.W.L.) and U01 NS108637 (awarded to J.W.L.). L.M.'s work was supported in part by a fellowship from MathWorks. T.L.A. is supported by the MIT-Novo Nordisk Artificial Intelligence Postdoctoral Fellows Program. This article is dedicated to our friend and colleague S.S. who sadly passed away earlier this year.

Author contributions

Y.M., I.S.C., C.F.P. and P.P. contributed equally to this work. Conceptualization: the original idea was conceived by Y.M., N.S., J.W.L. and A.D.T.S. The core methodology was invented by Y.M. Additional conceptual contributions were provided by D.R.B., H.P., L.M., M.P., P.P. and R. Schoenmakers. Methodology and software: Y.M. led the overall implementation. Y.M., I.S.C. and C.F.P. performed the main software development and experiments. P.P. assisted with the utilization of Thermo Fisher's API and contributed to experiments. R. Schalek and M.P. assisted with microscope operation. S.S. developed the EMInclude and EMExclude methods and, with T.L.A., performed neural network optimization. Y.L. developed the image homogenization method using GANs. L.M. provided access to an early version of the ML-based imaging methods. Data and validation: V.S. prepared the *C. elegans* sample, and N.K. provided the mouse cortex wafer. Y.W. performed data stitching and alignment. I.S.C., C.A.B., D.X., H.M., J.M. and B.A.W. validated the segmentation accuracy. D.R.B. created the visualizations. Supervision and writing: the project was supervised by J.W.L., A.D.T.S. and N.S. The paper was written by Y.M., I.S.C., J.W.L. and A.D.T.S. with significant writing contributions from S.S., Y.L. and T.L.A. and input from all authors.

Competing interests

P.P., M.P. and R. Schoenmakers are employees of Thermo Fisher Scientific. L.M. received funding from MathWorks. The other authors declare no competing interests.

Additional information

Extended data is available for this paper at https://doi.org/10.1038/s41592-025-02929-3.

Supplementary information The online version contains supplementary material available at https://doi.org/10.1038/s41592-025-02929-3.

Correspondence and requests for materials should be addressed to Yaron Meirovitch, Jeff W. Lichtman, Aravinthan D. T. Samuel or Nir Shavit.

Peer review information *Nature Methods* thanks the anonymous reviewers for their contribution to the peer review of this work. Primary Handling Editor: Nina Vogt, in collaboration with the *Nature Methods* team.

https://doi.org/10.1038/s41592-025-02929-3

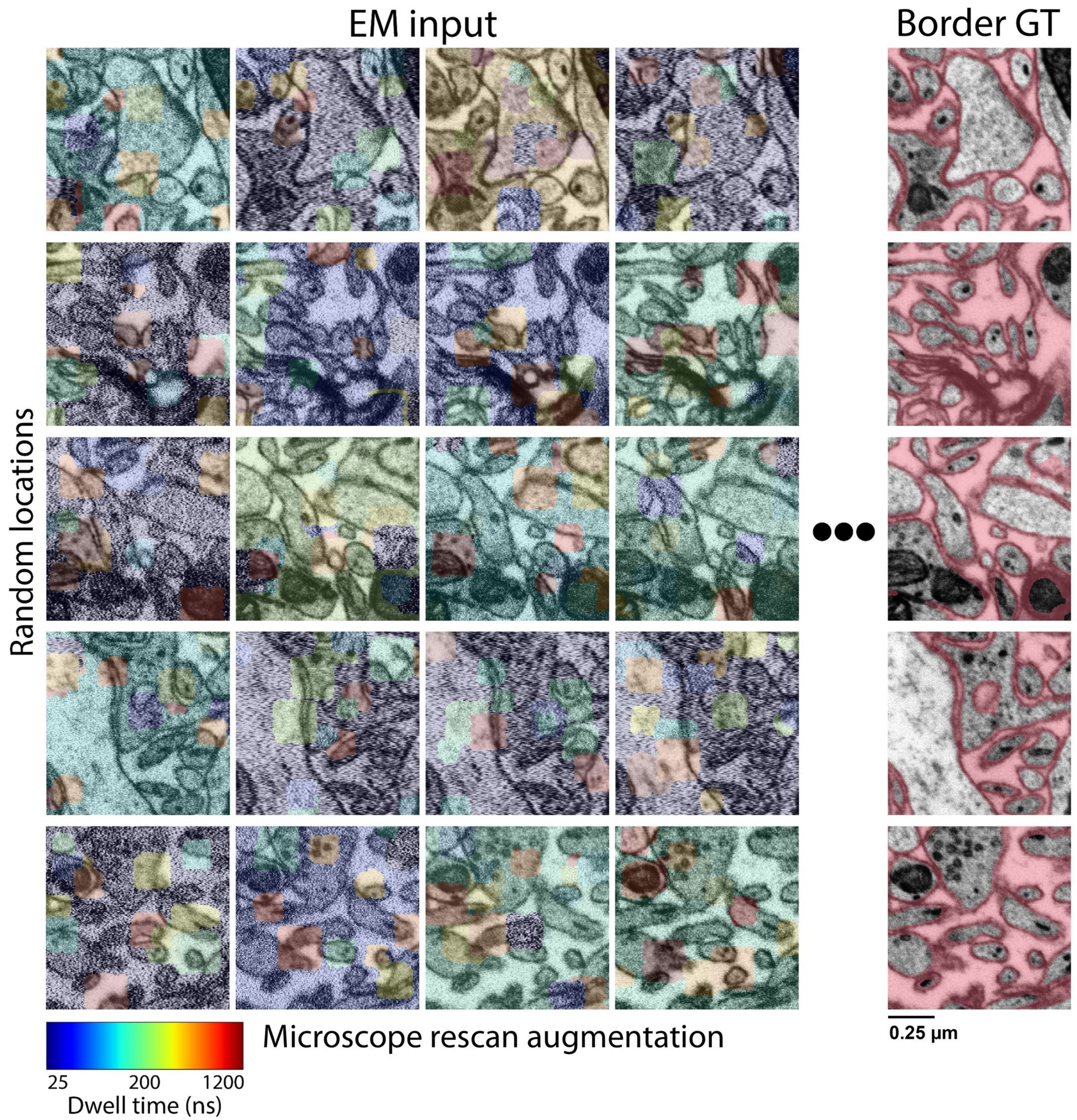

Extended Data Fig. 1 | Dwell time rescan data augmentation. Rows 1-5 show different locations in the EM sample. Columns 1-4 show different augmented composite images that were taken at different dwell times; short dwell time pixels in blue, representing 25 ns/pixel scans; long dwell time pixels in red, representing 1200 ns/pixel. Column 5 shows the ground truth classes for each region that were obtained from the long dwell time neural network (SLOW2EM).

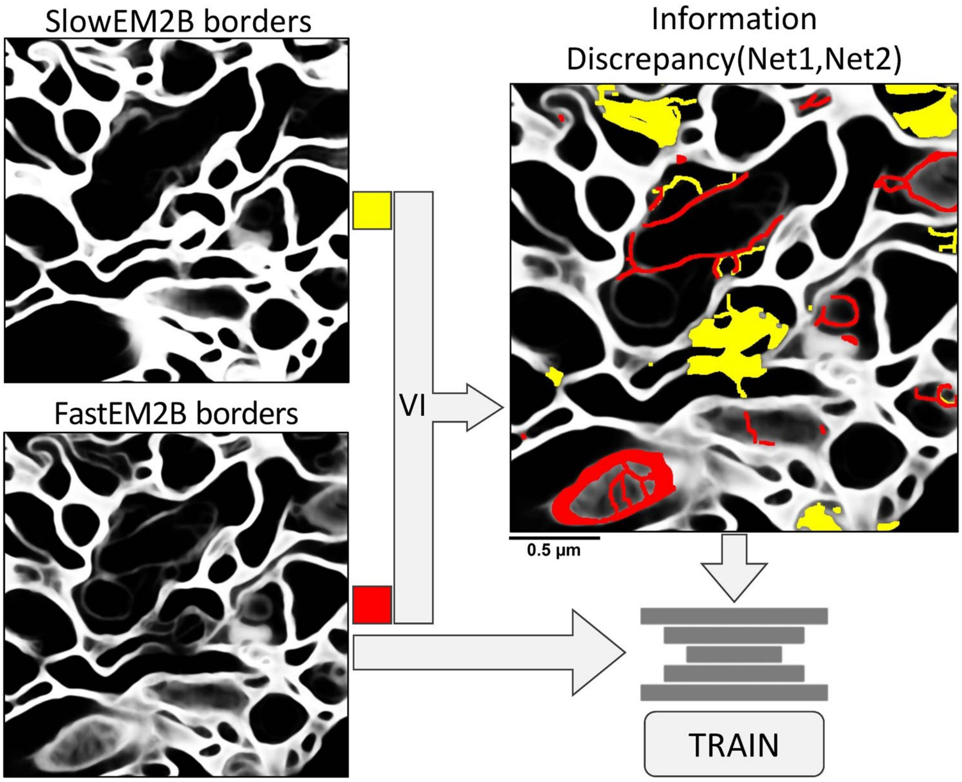

Extended Data Fig. 2 | The discrepancy between segmentation with long dwell time (using SLOWEM2B) and short dwell time (using FASTEM2B) based on VI. VI is the sum of individual error terms contributed by each object in the two segmented images. The most variable objects are flagged. Image processing is used to delineate specific borders that appear in only one segmented image. Yellow represents segmented objects that are uniquely predicted in the long dwell time image. Red represents segmented objects that are uniquely predicted in the short dwell time image. A neural network (ERRNET) is trained to predict all red and yellow discrepancies only using short dwell time images. This is possible because variation occurs where border predictors are uncertain and often with typical, at times biologically implausible, border prediction.

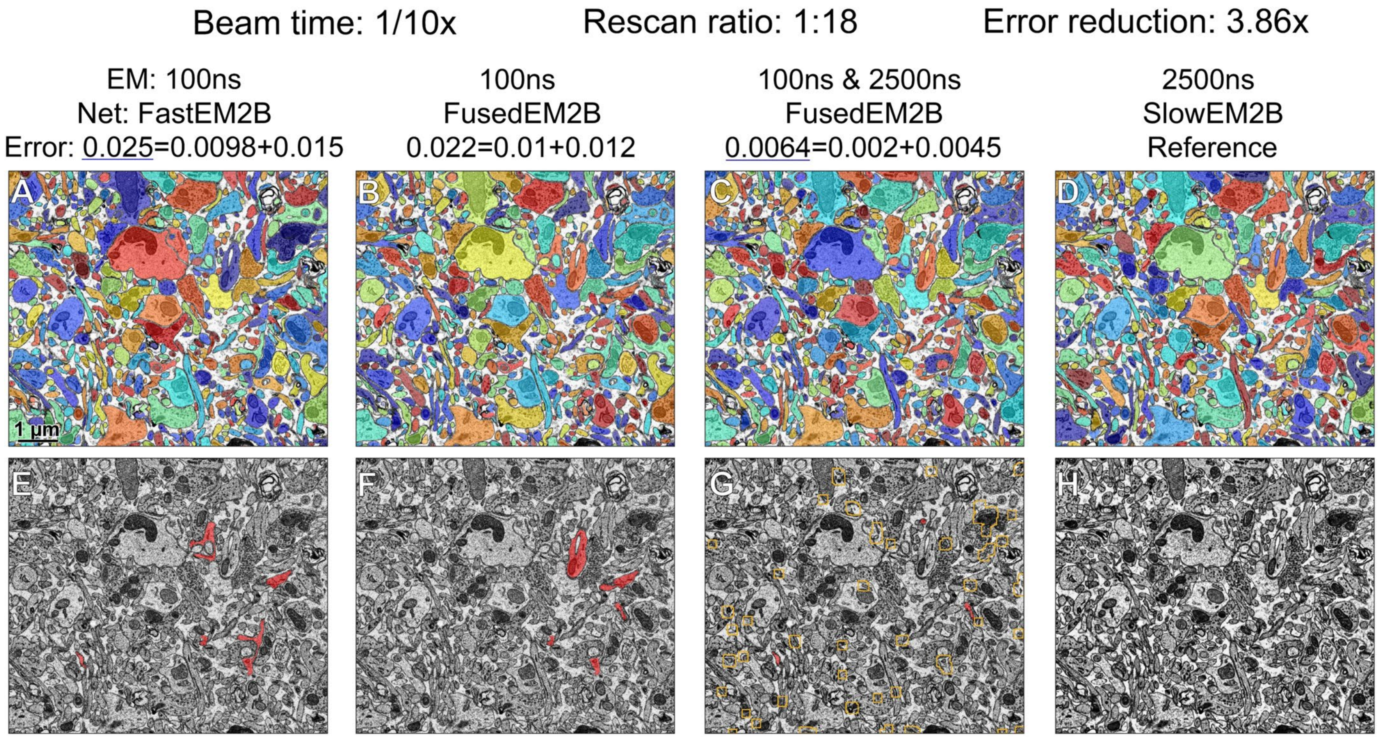

Extended Data Fig. 3 | Composite EM images fusing short and long dwell time regions are better segmented compared to short dwell time images. We tested in the mouse cortex datasets whether replacing short dwell time error-prone regions with longer dwell time scans improves the ability to segment. Error of the instance segmentation is assessed in terms of the Variation of Information (VI) compared to the segmented reference image, where VI is composed of a merge and split error terms as in equation (1).

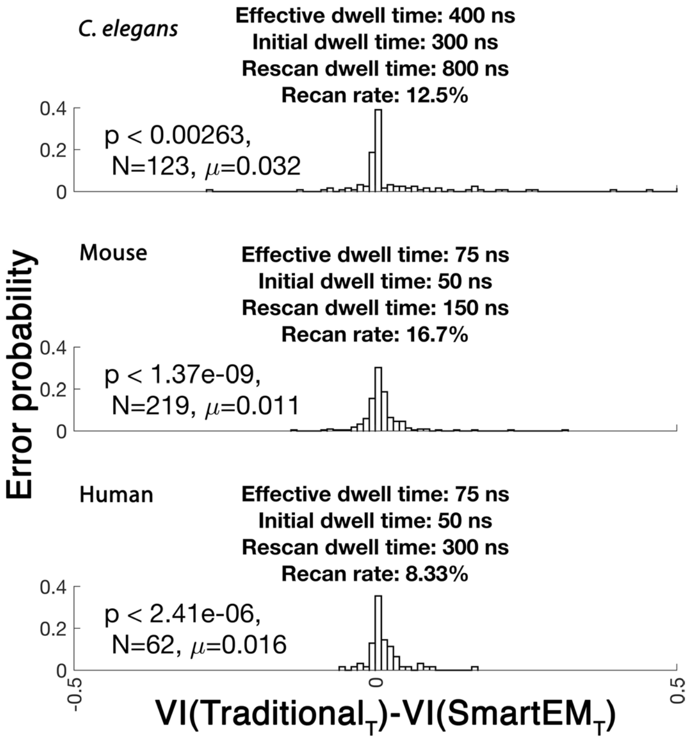

Extended Data Fig. 4 | Distribution of segmentation error differences (standard minus SmartEM) across datasets/species. The C. elegans nerve ring (top), mouse cortex (middle), and human temporal lobe (bottom) - each collected using a homogeneous and a time-matched SmartEM dwell time. Parameter settings for each case (effective dwell times, initial dwell times, rescan dwell times, and rescan rates) are shown in the panel titles. Each distribution plots the Variation of Information (VI) error from the standard pipeline minus that from SmartEM for a collection of N images; positive values indicate lower error in SmartEM.

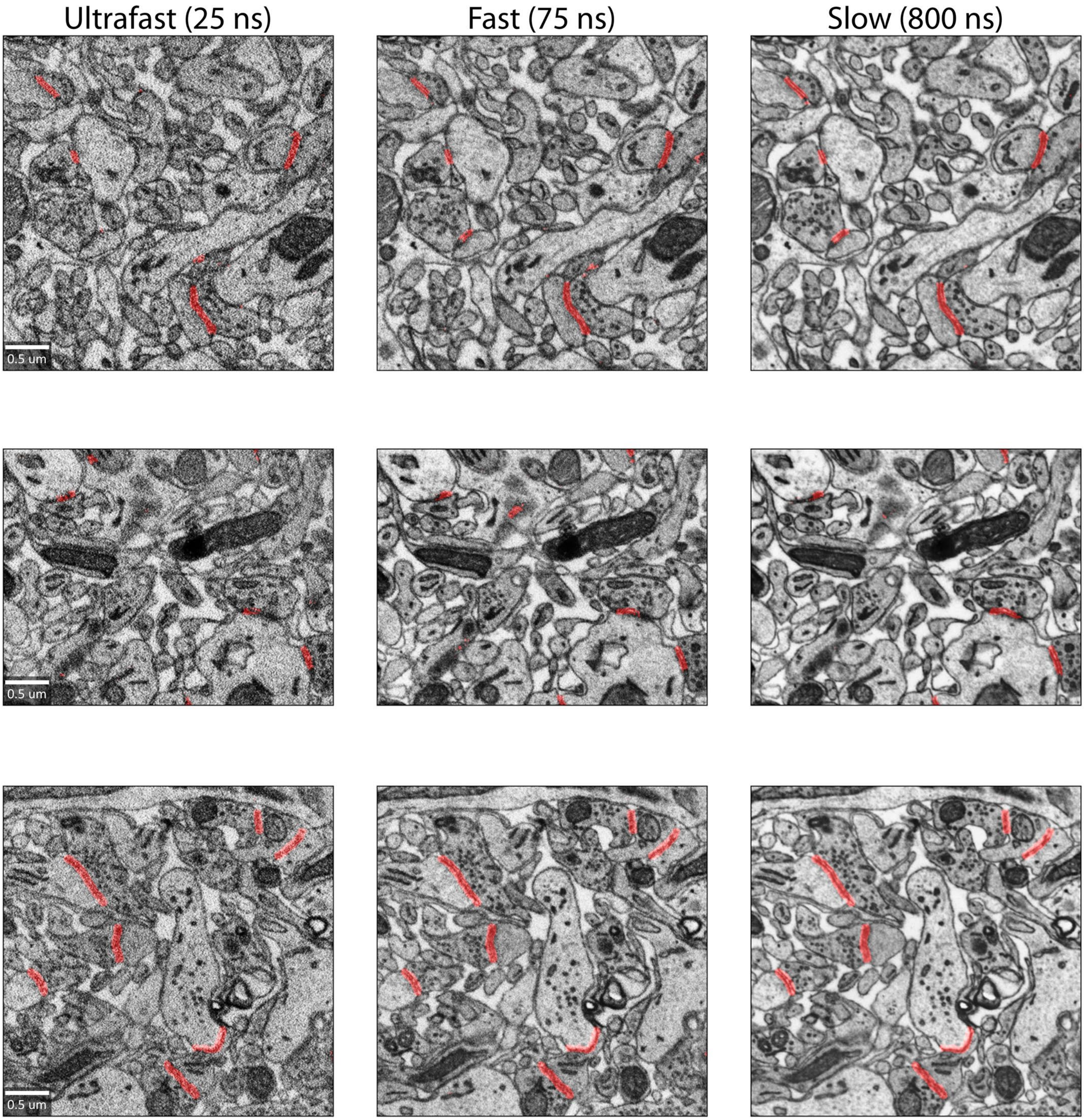

Extended Data Fig. 5 | Synapse detection in ultrafast (25 ns), fast (75 ns) and slow (800 ns) dwell time. The output of EMINCLUDE is depicted for multiple dwell times.

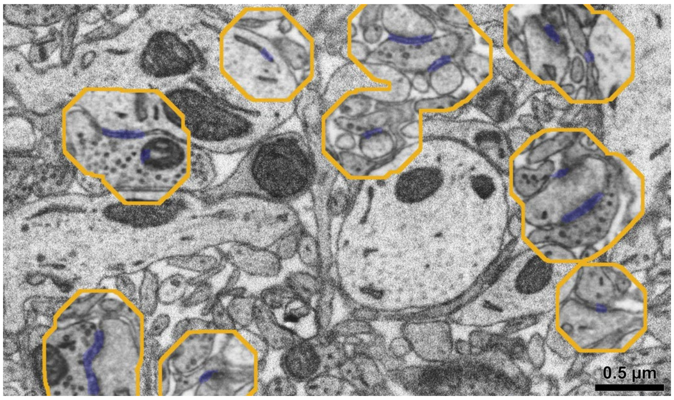

Extended Data Fig. 6 | Data-aware imaging of synapses at long dwell time. SmartEM takes a short dwell time image (50 ns/pixel), predicts locations that contain synapses, and rescans these regions at long dwell time (1200 ns/pixel). The blue overlay presents synapse predictions by EMINCLUDE. Yellow outlines represent locations for rescan based on dilation of EMINCLUDE predictions.

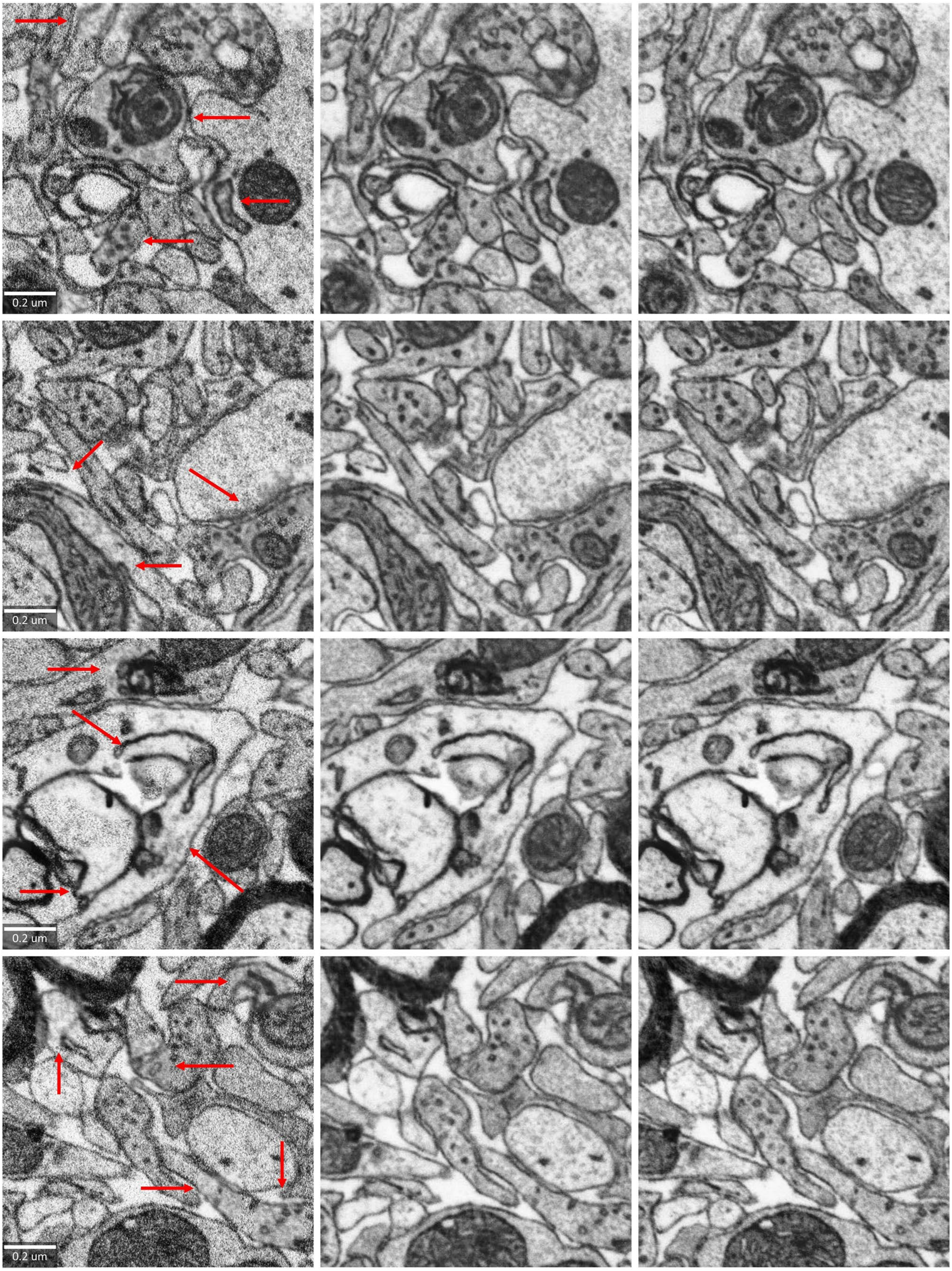

Extended Data Fig. 7 | Examples of image homogenization by IMAGEHOMOGENIZER. Left column: composite EM with two dwell times (75 ns/pixel and 600 ns/pixel). Middle column: homogenized EM from composite EM. Right column: slow EM (600 ns/pixel). Red arrows indicate the locations with slow dwell time of 600 ns/pixel in composite EM.

nature portfolio

Corresponding author(s): Yaron Meirovitch, Jeff Lichtman, Aravinthan Samuel

Last updated by author(s): Sep 25, 2025

Reporting Summary

Nature Portfolio wishes to improve the reproducibility of the work that we publish. This form provides structure for consistency and transparency in reporting. For further information on Nature Portfolio policies, see our Editorial Policies and the Editorial Policy Checklist.

Statistics

For all statistical analyses, confirm that the following items are present in the figure legend, table legend, main text, or Methods section.

n/a	Confirmed	
☐	☒	The exact sample size (*n*) for each experimental group/condition, given as a discrete number and unit of measurement
☐	☒	A statement on whether measurements were taken from distinct samples or whether the same sample was measured repeatedly
☐	☒	The statistical test(s) used AND whether they are one- or two-sided *Only common tests should be described solely by name; describe more complex techniques in the Methods section.*
☒	☐	A description of all covariates tested
☐	☒	A description of any assumptions or corrections, such as tests of normality and adjustment for multiple comparisons
☐	☒	A full description of the statistical parameters including central tendency (e.g. means) or other basic estimates (e.g. regression coefficient) AND variation (e.g. standard deviation) or associated estimates of uncertainty (e.g. confidence intervals)
☐	☒	For null hypothesis testing, the test statistic (e.g. F, t, r) with confidence intervals, effect sizes, degrees of freedom and P value noted *Give P values as exact values whenever suitable.*
☒	☐	For Bayesian analysis, information on the choice of priors and Markov chain Monte Carlo settings
☒	☐	For hierarchical and complex designs, identification of the appropriate level for tests and full reporting of outcomes
☐	☒	Estimates of effect sizes (e.g. Cohen's d, Pearson's r), indicating how they were calculated

Our web collection on statistics for biologists contains articles on many of the points above.

Software and code

Policy information about availability of computer code

Data collection	We used Thermo Fisher "AutoScript 4" API combined with Python and MATLAB to control the microscope. Collections was aided with in-house trained models in MATLAB and PyTorch.
Data analysis	We analyzed the data in MATLAB and Python.

For manuscripts utilizing custom algorithms or software that are central to the research but not yet described in published literature, software must be made available to editors and reviewers. We strongly encourage code deposition in a community repository (e.g. GitHub). See the Nature Portfolio guidelines for submitting code & software for further information.

Data

Policy information about availability of data

All manuscripts must include a data availability statement. This statement should provide the following information, where applicable:

- Accession codes, unique identifiers, or web links for publicly available datasets
- A description of any restrictions on data availability
- For clinical datasets or third party data, please ensure that the statement adheres to our policy

All SmartEM datasets and machine learning models are publicly available through a \href{https://doi.org/10.60533/boss-2023-4w35}{BossDB Project Page} (The Brain Observatory Storage Service and Database) \citep{hider_bossdb}.

Research involving human participants, their data, or biological material

Policy information about studies with human participants or human data. See also policy information about sex, gender (identity/presentation), and sexual orientation and race, ethnicity and racism.

Reporting on sex and gender	N/A
Reporting on race, ethnicity, or other socially relevant groupings	N/A
Population characteristics	N/A
Recruitment	N/A
Ethics oversight	N/A

Note that full information on the approval of the study protocol must also be provided in the manuscript.

Field-specific reporting

Please select the one below that is the best fit for your research. If you are not sure, read the appropriate sections before making your selection.

☒ Life sciences ☐ Behavioural & social sciences ☐ Ecological, evolutionary & environmental sciences

For a reference copy of the document with all sections, see nature.com/documents/nr-reporting-summary-flat.pdf

Life sciences study design

All studies must disclose on these points even when the disclosure is negative.

Sample size	We collected datasets from three organisms and segmented them across an entire wafer. For each specimen we conducted analyses within sample across different separated areas, randomly picked from all sections. The number of sections used to derive the statistics was chosen based on the imaging time and the speedup analysis parameters, both are slow procedures due to the slow pace of EM imaging and the large augmentation of the ML models. In any event, we made sure N was larger than the number of sections but without repeatidly sampling from the same section to maximize variability.
Data exclusions	Blurry images were excluded from the speedup analysis or areas that do not contain neuropil that is relevant for the connectomics question.
Replication	Our data are available for segmentation experiments, and wafers can be re-imaged for reproducibility purposes.
Randomization	We heavily relied on randomization both of the section ID and the X/Y location within a section.
Blinding	Investigators who rejected blurry images were not aware of the effect these regions would have on speedup.

Reporting for specific materials, systems and methods

We require information from authors about some types of materials, experimental systems and methods used in many studies. Here, indicate whether each material, system or method listed is relevant to your study. If you are not sure if a list item applies to your research, read the appropriate section before selecting a response.

Materials & experimental systems

n/a	Involved in the study
☒	☐ Antibodies
☒	☐ Eukaryotic cell lines
☒	☐ Palaeontology and archaeology
☐	☒ Animals and other organisms
☒	☐ Clinical data
☒	☐ Dual use research of concern
☒	☐ Plants

Methods

n/a	Involved in the study
☒	☐ ChIP-seq
☒	☐ Flow cytometry
☒	☐ MRI-based neuroimaging

Animals and other research organisms

Policy information about studies involving animals; ARRIVE guidelines recommended for reporting animal research, and Sex and Gender in Research

Laboratory animals	We used a male C. elegans, N2 Bristol strain. Other data in this study were based on animal preparation from previous studies.
Wild animals	N/A
Reporting on sex	Sex was not considered.
Field-collected samples	N/A
Ethics oversight	No ethical guidance needed for C. elegans.

Note that full information on the approval of the study protocol must also be provided in the manuscript.

Plants

Seed stocks	N/A
Novel plant genotypes	N/A
Authentication	N/A